The Journal of Clinical Investigation

Dysfunction of the ciliary ARMC9/TOGARAM1 protein module causes Joubert syndrome

Brooke L. Latour, … , Ronald Roepman, Dan Doherty

J Clin Invest. 2020. https://doi.org/10.1172/JCI131656.

Research In-Press Preview **Genetics**

Joubert syndrome (JBTS) is a recessive neurodevelopmental ciliopathy, characterized by a pathognomonic hindbrain malformation. All known JBTS-genes encode proteins involved in the structure or function of primary cilia, ubiquitous antenna-like organelles essential for cellular signal transduction. Here, we use the recently identified JBTS-associated protein ARMC9 in tandem-affinity purification and yeast two-hybrid screens to identify a novel ciliary module whose dysfunction underlies JBTS. In addition to known JBTS-associated proteins CEP104 and CSPP1, we identify CCDC66 and TOGARAM1 as ARMC9 interaction partners. We show that TOGARAM1 variants cause JBTS and disrupt TOGARAM1 interaction with ARMC9. Using a combination of protein interaction analyses and characterization of patient-derived fibroblasts, CRISPR/Cas9-engineered zebrafish and hTERT-RPE1 cells, we demonstrate that dysfunction of *ARMC9* or *TOGARAM1* results in short cilia with decreased axonemal acetylation and polyglutamylation, but relatively intact transition zone function. Aberrant cold- and serum-induced ciliary loss in both *ARMC9* and *TOGARAM1* patient cell lines suggests a role for this new JBTS-associated protein module in ciliary stability.

Dysfunction of the ciliary ARMC9/TOGARAM1 protein module causes Joubert syndrome

Author list

Brooke L. Latour (1)*, Julie C. Van De Weghe (2)*, Tamara D.S. Rusterholz (3,4)*, Stef J.F. Letteboer (1), Arianna Gomez (2), Ranad Shaheen (5), Matthias Gesemann (4), Arezou Karamzade (6), Mostafa Asadollahi (6), Miguel Barroso-Gil (7), Manali Chitre (8), Megan E. Grout (2), Jeroen van Reeuwijk (1), Sylvia E.C. van Beersum (1), Caitlin V. Miller(2), Jennifer C. Dempsey (2), Heba Morsy (9), University of Washington Center for Mendelian Genomics (10), Michael J. Bamshad (2,10,11), Genomics England Research Consortium (12), Deborah A. Nickerson (10,11), Stephan C.F. Neuhauss (4), Karsten Boldt (13), Marius Ueffing (13), Mohammad Keramatipour (6), John A. Sayer (7), Fowzan S. Alkuraya (5,14), Ruxandra Bachmann-Gagescu (3,4)*, Ronald Roepman (1)* & Dan Doherty (2,15)*

Affiliations

1) Department of Human Genetics and Radboud Institute for Molecular Life Sciences, Radboud University Medical Center, Geert Grooteplein Zuid 10, 6525 GA Nijmegen, The Netherlands
2) Department of Pediatrics, University of Washington, Seattle, WA, 98195 USA
3) Institute of Medical Genetics, University of Zurich, 8952 Schlieren, Switzerland
4) Department of Molecular Life Sciences, University of Zurich, 8057 Zürich, Switzerland
5) Department of Genetics, King Faisal Specialist Hospital and Research Center, Riyadh, Saudi Arabia
6) Department of Medical Genetics, Faculty of Medicine, Tehran University of Medical Sciences, Tehran 14179 13151, Iran
7) Translational and Clinical Research Institute, Faculty of Medical Sciences, Newcastle University, Newcastle Upon Tyne, UK

8) Department of Paediatric Neurology, Cambridge University Hospitals NHS Foundation Trust, Cambridge, UK.
9) Department of Human Genetics, Medical Research Institute, Alexandria University, Alexandria, Egypt
10) University of Washington Center for Mendelian Genomics, Seattle, WA 98195, USA
11) Department of Genome Sciences, University of Washington, Seattle, WA 98195, USA
12) Genomics England, London, EC1M 6BQ, United Kingdom
13) Medical Proteome Center, Institute for Ophthalmic Research, University of Tuebingen, 72074 Tuebingen, Germany
14) Department of Anatomy and Cell Biology, College of Medicine, Alfaisal University, Riyadh 11533, Saudi Arabia
15) Center for Integrative Brain Research, Seattle Children's Research Institute, Seattle, WA, 98101 USA

*These authors contributed equally to this work.

Correspondence and requests for materials should be addressed to R.B.G. (email: ruxandra.bachmann@imls.uzh.ch) or to R.R. (email: ronald.roepman@radboudumc.nl) or to D.D. (email: ddoher@uw.edu).

The authors declare that no conflict of interest exists.

Abstract

Joubert syndrome (JBTS) is a recessive neurodevelopmental ciliopathy, characterized by a pathognomonic hindbrain malformation. All known JBTS-genes encode proteins involved in the structure or function of primary cilia, ubiquitous antenna-like organelles essential for cellular signal transduction. Here, we used the recently identified JBTS-associated protein ARMC9 in tandem-affinity purification and yeast two-hybrid screens to identify a ciliary module whose dysfunction underlies JBTS. In addition to known JBTS-associated proteins CEP104 and CSPP1, we identified CCDC66 and TOGARAM1 as ARMC9 interaction partners. We found that *TOGARAM1* variants cause JBTS and disrupt TOGARAM1 interaction with ARMC9. Using a combination of protein interaction analyses and characterization of patient-derived fibroblasts, CRISPR/Cas9-engineered zebrafish and hTERT-RPE1 cells, we demonstrated that dysfunction of *ARMC9* or *TOGARAM1* result in short cilia with decreased axonemal acetylation and polyglutamylation, but relatively intact transition zone function. Aberrant serum-induced ciliary resorption and cold-induced depolymerization in *ARMC9* and *TOGARAM1* patient cell lines suggest a role for this new JBTS-associated protein module in ciliary stability.

Word count: 159

Introduction

Ciliopathies are a heterogeneous class of disorders that arise from defects in the structure or function of the primary cilium (1, 2), a highly specialized microtubule-based sensory organelle that protrudes from the surface of most eukaryotic cell types (3). Joubert syndrome (JBTS) is a recessive, genetically heterogeneous, neurodevelopmental ciliopathy, defined by a distinctive brain malformation, recognizable as the "molar tooth sign" (MTS) (4) in axial magnetic resonance images through the midbrain-hindbrain junction. Affected individuals have hypotonia, ataxia, abnormal eye movements, and cognitive impairment. Additional features can occur, including retinal dystrophy, fibrocystic kidney disease, liver fibrosis, polydactyly, and coloboma (5). To date, variants in more than 35 genes have been causally linked to JBTS, but the genetic diagnosis cannot be identified in all patients, and the disease mechanisms remain unclear (6–8).

All JBTS-associated proteins identified thus far function in and around the primary cilium, but their dysfunction can affect a wide variety of cellular processes, including cilium formation, resorption, tubulin post-translational modifications, membrane phosphatidylinositol composition, ciliary signaling pathways, actin cytoskeleton dynamics, and DNA damage response signaling (9–14). Many JBTS proteins act together in complexes that localize to specific subdomains of the ciliary compartment. Disruption of the composition, architecture, or function of these ciliary subdomains causes disease (6).

The core of the cilium is composed of nine microtubule doublets forming the ciliary axoneme, which is anchored to the cell by the basal body, a modified centriole. The axonemal microtubules undergo a range of post-translational modifications including polyglutamylation and acetylation which are important for the structure and function of the cilium (15–17). The ciliary membrane has a distinct protein and lipid distribution that differs from the contiguous plasma membrane. This unique composition is achieved in part by the transition zone (TZ) that connects the axoneme to the membrane and acts as a partition. Approximately half of the known JBTS proteins, including RPGRIP1L (JBTS7) (18, 19) and CC2D2A (JBTS9) (20), assemble into multi-protein complexes at the ciliary TZ where they organize the molecular gate that regulates ciliary protein entry and exit (21); TZ dysfunction is thought to play a key role in JBTS (22). Another subset of JBTS-associated proteins, including ARL13B (JBTS8) (23) and INPP5E (JBTS1) (10), associate with the ciliary membrane distal to the TZ. These proteins are thought to regulate signaling pathways such as Hedgehog (Hh) by modulating ciliary protein and lipid composition (24, 25). Different JBTS-associated proteins have been found to function at the basal body or distal segment/tip (6). CSPP1 (JBTS 21) (26, 27) and CEP104 (JBTS25) (28) are mainly detected at the centrosomes and ciliary basal bodies; however, their exact molecular function, and how defects in these proteins lead to JBTS, are less well understood. CEP104 localizes to the ciliary tip during ciliogenesis, where it is required for structural integrity in the motile cilia of *Chlamydomonas* and *Tetrahymena* (29, 30). Pathogenic variants in the gene encoding the ciliary tip kinesin KIF7 (JBTS12) also cause JBTS, and KIF7 dysfunction has been linked to defects in tubulin acetylation and Hh signaling (31).

Recently, we identified biallelic pathogenic *ARMC9* (armadillo repeat motif containing 9) variants in individuals with JBTS (JBTS30). ARMC9 localizes to centrioles (32) and the proximal portion of the cilium (33) in mammalian cilia. *ARMC9* transcript levels are upregulated with induction of ciliogenesis, and *armc9* dysfunction in zebrafish yields typical ciliopathy phenotypes (32). ARMC9 has not been identified as a component of the ciliary JBTS-associated protein complexes mentioned above, so in this work, we used ARMC9 as bait in protein interaction screens. These screens identified a microtubule-associated ciliary protein module containing multiple other JBTS-associated proteins (CEP104, CSPP1, RPGRIP1L, and CEP290) and two other ciliary proteins (TOGARAM1 and CCDC66) not previously implicated in JBTS. Strikingly, we identified biallelic pathogenic *TOGARAM1* variants as the cause of JBTS in five families. To decipher the function of the ARMC9-TOGARAM1 protein module and assess its role in the pathology of JBTS, we mapped the interaction domains and evaluated cellular defects in cultured human cells and zebrafish mutants. We find that these proteins, previously shown to associate with microtubules (29, 34–36), are required for appropriate post-translational modification of ciliary microtubules and cilium stability.

Results

Identification of a novel protein module implicated in JBTS

We performed protein interaction screens to define the ARMC9-associated interactome. To identify direct binding partners, we employed full-length ARMC9 and four fragments (Figure 1A) as bait in a GAL4-based yeast two-hybrid (Y2H) interaction trap screen of two validated prey retinal cDNA libraries that were generated via random or oligo-dT primers (37). Using full-length ARMC9 as a bait, we identified four proteins previously implicated in ciliary function as binary interactors, including ARMC9 itself (suggesting a propensity to multimerize), TOGARAM1 (29, 34), CCDC66 (36, 38), and the JBTS-associated protein CSPP1 (39). Validation of these interactions and evaluation of the interacting domains was performed by Y2H co-expression. This assay indicated that the potential self-binding propensity of ARMC9 is mediated by fragment 2 containing the N-terminal 350 amino acid stretch containing the lissencephaly type-1-like homology motif (LisH) and coiled-coil domains, while TOGARAM1 and CSPP1 associated with fragment 4 (150-665 aa) containing the coiled-coil domain and the armadillo repeats domain (Figure 1B, C). We also used full-length TOGARAM1 and three fragments (Figure 1D) in parallel screens which confirmed the direct interaction between TOGARAM1 and ARMC9 (Figure 1E), and yielded an additional candidate interactor, the JBTS-associated transition zone protein RPGRIP1L (JBTS7) (Figure 1E). The interaction with ARMC9 was mapped to the N-terminal portion of TOGARAM1 (fragment 1) containing the TOG1 and TOG2 domains, while RPGRIP1L bound to the linker region (fragment 2) between the TOG2 and TOG3 domain (Figure 1E).

To identify ARMC9-associated protein complexes, we expressed strep – FLAG epitope-tagged ARMC9 in HEK293T cells, followed by tandem affinity purification (TAP) and subsequent mass spectrometry. This identified 106 candidate ARMC9 interactors, including TOGARAM1 and the JBTS-associated protein CEP290 (Figure 1G, H; Supplemental table 1). Subsequent TAP experiments using tagged TOGARAM1, CCDC66, and CSPP1 confirmed the presence of ARMC9 in the TOGARAM1 and CCDC66 complexes, and extended the network to include several other ciliary proteins (Supplemental tables 2-4). For TOGARAM1, these additional candidate interactors included ciliary proteins ARMC9, CEP104, IFT74, IFT172, PLK1, and PRPF31, (Supplemental table 2), for CCDC66, they included ARMC9 and DYNLL1 (Supplemental table 3), and for CSPP1, they included RPGRIP1L and CEP290 (Supplemental table 4).

To further validate the ARMC9 interactors identified in TAP and Y2H experiments and evaluate their propensity to interact, we performed reciprocal co-IPs of all binary permutations of the module components ARMC9, TOGARAM1, CEP104, CCDC66, and CSPP1 (Figure 1F, Supplemental Figure 1A-I). The results confirmed the interaction of ARMC9 with TOGARAM1, CCDC66, CEP104, and CSPP1 (Figure 1G). Additionally, we performed PalmMyr-CFP mislocalization assays to further confirm the interaction of TOGARAM1 and ARMC9. The PalmMyr-CFP assay utilizes a PalmMyr tag which provides sites for palmitoylation and myristoylation. The palmitoylation and myristoylation forces the tagged protein to (mis)localize to the cell membrane (40). This mislocalization can be evaluated by fluorescence microscopy of CFP signal. We transfected PalmMyr-CFP tagged ARMC9 and mRFP-tagged TOGARAM1 into human telomerase reverse transcriptase retina pigmented epithelium (hTERT-RPE1) cells, alone and in combination, to assess the interaction between ARMC9 and TOGARAM1. Cells transfected with PalmMyr-

CFP-ARMC9 alone showed diffuse localization across the cell membrane (Supplemental Figure 1B), while mRFP-TOGARAM1 alone localized to microtubule-like structures (Supplemental Figure 1C). Co-expression yielded complete co-localization along these structures despite the PalmMyr tag on ARMC9 (Supplemental Figure 1D), thereby indicating a direct interaction of the two proteins and a likely strong microtubule binding affinity of TOGARAM1.

***TOGARAM1* variants cause JBTS in humans**

Next, we investigated whether our interactome dataset could be used to identify new JBTS-associated genes. We cross-referenced the ARMC9-interactome data with DNA sequence data from our cohort of >600 families affected by JBTS (41). We first evaluated exome sequence data for 53 individuals in 51 families without variants in known JBTS genes. We identified biallelic, missense *TOGARAM1* variants in a fetus with cerebellar vermis hypoplasia and polydactyly (UW351-3 in Figure 2A and Table 1). These variants (c.1124T>C; p.Leu375Pro and c.3931C>T; p.Arg1311Cys) are rare in gnomAD v2.1 (42) and predicted to be deleterious by combined annotation dependent depletion (CADD) (43) (Table 1). To identify additional families, we sequenced all of the known JBTS genes using small-molecule molecular inversion probe capture (44) in 534 additional individuals from the same cohort and identified another individual (UW360-3 in Table 1 and Figure 2A) with the molar tooth sign (Figure 2B) and a nonsense variant (c.1084C>T; p.Gln362*) on one allele and low read depth indicating a possible multi-exon deletion event on the other allele. We confirmed a 12 kb deletion using a custom comparative genomic hybridization array, and fibroblast cDNA sequencing revealed deletion of exons 4-7 (Figure 2C). Genomic DNA sequencing of the proband and parents revealed that the 12,191 base pair deletion was inherited from the father (Figure 2C). In parallel, exome sequencing in several other cohorts of individuals with ciliopathy and neurodevelopmental conditions identified three other individuals with *TOGARAM1*-related JBTS (Table 1 and Figure 2A, B): 13DG1578 (consanguineous) with a homozygous rare, predicted-deleterious missense variant (c.1102C>T; p.Arg368Trp), WGL-1914 (consanguineous) with a rare, homozygous stop-gain variant (c.3248C>A; p.Ser1083*), and JAS-L50 (non-consanguineous) with rare, compound heterozygous missense and stop-gain variants (c.1112C>A; p.Ala371Asp and c.5023C>T; p.Arg1675*). Most variants identified in this work cluster around the TOG (tumor overexpressed gene) domains in the protein (Figure 2D). TOGARAM1 is also known as FAM179B and KIAA0423, with homologs CHE-12 in *C.elegans* and Crescerin1 in mouse. Segregation analysis for all affected families confirmed a recessive inheritance pattern (Figure 2A and Supplemental Figure 3).

The five affected individuals had features consistent with JBTS, including classic brain imaging findings (absent cerebellar vermis and thick, horizontally oriented superior cerebellar peduncles, giving the appearance of the molar tooth sign) in the four children (Figure 2B), and cerebellar vermis hypoplasia in the fetus (UW351-3). This fetus also had bilateral postaxial foot polydactyly and abnormal craniofacial features at autopsy including broad nasal bridge and posteriorly rotated ears. The four living children have typical hypotonia, ataxia, cognitive delays and behavioral features associated with JBTS, while WGL-1914 and JAS-L50 had kidney involvement and WGL-1914 also had liver involvement. Uncommonly seen in individuals with JBTS, widely spaced nipples, male genital abnormalities (undescended testicles and possible micropenis in UW360-3, and small scrotum and testicle in 13DG1578), and somewhat similar dysmorphic features were noted in several of these individuals (Table 1).

JBTS-associated *TOGARAM1* missense variants in the TOG2 domain disrupt the ARMC9-TOGARAM1 interaction

TOGARAM1 is a member of the highly conserved FAM179 protein family and is found across ciliated eukaryotes including *Chlamydomonas reinhardtii*, *Tetrahymena thermophila*, and *Caenorhabditis elegans*. TOGARAM1 has four conserved TOG domains that display similarity to the tubulin binding domains in ch-TOG and CLASP family proteins (34). Arg368Trp, Ala371Asp, and Leu375Pro, lie within the highly conserved TOG2 domain (Figure 2D, Supplemental Figure 2A) which has been found to promote microtubule polymerization in vitro (34). The TOG2 domain conforms to the canonical TOG domain architecture found in other TOG array containing proteins such as CLASP and Stu2 (Supplemental Figure 2A), therefore disruption of this domain is predicted to disturb microtubule binding (45). Using in silico analysis of the effects of point mutations, we found that Arg368Trp, Ala371Asp, and Leu375Pro, variants were predicted to be deleterious to protein structure (45). Residue 368 is highly conserved, modeling the wild-type and mutant TOG domains using HOPE (45) predicts that the larger and neutral tryptophan disrupts the normal hydrogen bonds with the aspartic acid residues at positions 361 and 405 (Supplemental Figure 2B, C). Position 371 is highly conserved, and due to the difference in size and hydrophobicity, aspartic acid at this position is predicted to disrupt the structure and function of the HEAT4 domain. Position 375 is located in a predicted α-helix, and is highly conserved; proline at this position is predicted to disrupt this α-helix as it introduces a bend in the polypeptide chain (Supplemental Figure 2D, E), likely affecting protein folding or interaction with other domains (45).

To assess the effects of JBTS-associated missense variants, we modeled two of the TOG2 domain variants (Arg368Trp, Leu375Pro) and the single TOG3 domain variant (Arg1311Cys) by expressing wild-type and mutant mRFP-tagged TOGARAM1 in control (Figure 3A-E) and genetically edited *TOGARAM1* mutant hTERT-RPE lines (Supplemental Figure 4A, B). The genetically edited *TOGARAM1* mutant hTERT-RPE line, *TOGARAM1* mut 1, has a biallelic deletion of the ATG site of TOGARAM1 (Supplemental Figure 5A, B). Overexpressed wild-type TOGARAM1 localized along the ciliary axoneme and was associated with markedly longer cilia compared to untransfected wild-type cells (Figure 3A, B) and *TOGARAM1* mut 1 cells (Supplemental Figure 4A,B). Exogenous TOGARAM1 harboring these three variants individually also localized to the cilium, but overexpression of TOG2-domain variants Arg368Trp and Leu375Pro resulted in longer cilia while overexpression of the TOG3-domain variant Arg1311Cys resulted in shorter cilia compared to untransfected cells (Figure 3A-E, quantification in Figure 3F). These data suggest that disruption of the TOG3 domain may have a dominant negative effect on the microtubule polymerization capacity of TOGARAM1 and disruption of the TOG3 domain has a different effect on TOGARAM1 localization and ciliary extension as compared to TOG2 domain variants.

We next investigated the effects of the *TOGARAM1* variants on the interaction with ARMC9 using co-IP, binary yeast two-hybrid (Y2H) interaction analysis, and PalmMyr colocalization assays. We found that the variants in the TOG2 domain (Arg368Trp and Leu375Pro) abolished co-IP of HA-ARMC9 with Myc-TOGARAM1, while the Arg1311Cys variant in the TOG3 domain does not influence the interaction in these assays (Figure 3G). Y2H analysis confirmed these binary interactions (Figure 3H). In PalmMyr assays, the individually-expressed wild-type and mutant mRFP-tagged TOGARAM1 proteins localized along the length of cilia and along cytoplasmic microtubules (Supplemental Figure 4D). Co-expression of PalmMyr-CFP tagged ARMC9 with wild-type or Arg1311Cys mRFP-TOGARAM1 resulted in a pattern consistent with co-localization to cytoplasmic microtubules (Supplemental Figure 4E), indicating protein-protein interaction. In contrast, co-expression with the TOG2 variants resulted in PalmMyr-CFP tagged ARMC9 remaining localized to the plasma membrane, suggesting a lack of interaction with the TOGARAM1 mutants affecting the TOG2 domain (Supplemental Figure 4E). Taken together, these data indicate that variants in the TOG2 domain abrogate the ARMC9-TOGARAM1 interaction.

togaram1 **mutations cause ciliopathy phenotypes in zebrafish**

To further investigate the function of TOGARAM1 and the association between TOGARAM1 dysfunction and JBTS, we turned to zebrafish, an established model organism for ciliopathies. Indeed, zebrafish display a variety of ciliated cell types similar to humans, and pathogenic variants in human ciliopathy genes result in typical ciliopathy phenotypes in zebrafish. Ciliated cells typically assessed in the zebrafish model include epithelial cells in pronephric (kidney) ducts, olfactory neurons in nose pits or neuronal progenitors on larval brain ventricular surfaces.

We identified a single zebrafish *togaram1* ortholog displaying a highly conserved C-terminal region encompassing two TOG domains (similar to human TOG3 and 4) and a single N-terminal TOG domain corresponding to mammalian TOG2 domain (Supplemental Figure 6A). The three TOG domains are well-conserved between zebrafish and its corresponding human counterparts (50-58% amino acid identity and 72-77% similarity). As for the linker region between TOG domains, while it is more poorly conserved, it is enriched in serines and lysines (125 of 589 residues are Ser or Lys), similar to the proportion found in the human protein (165 of 657 residues are Ser or Lys); this is a common feature of TOG-domain containing proteins (46). Gene synteny analysis confirmed that the identified zebrafish sequence represents the ortholog of human *TOGARAM1* (Supplemental Figure 6B). Importantly, on the paralogous chromosomal fragment generated by the teleost-specific whole genome duplication, no second *togaram1* paralog could be identified. Moreover, synteny analysis also revealed that the zebrafish genome lacks a *TOGARAM2* ortholog (Supplemental Figure 6C), leaving zebrafish with just one *togaram* ortholog. These findings support the utility of zebrafish as a model for *TOGARAM1*-associated human disease.

We next generated zebrafish mutants using CRISPR/Cas9. Two different pairs of sgRNAs targeting different regions of the gene (Supplemental Figure 6D) led to similar phenotypes in injected F0 larvae. 39% developed a curved body shape and 9% developed kidney cysts, both typical zebrafish ciliopathy-associated phenotypes (Supplemental Figure 6E). Single larvae genotyping revealed a very high mutation efficiency (94% of sequenced clones from 7 larvae had small insertions-deletions, the majority of which were frameshift mutations). Mutant F0 fish displayed a striking scoliosis phenotype as juveniles (Supplemental Figure 6E), reminiscent of other ciliopathy mutants including *armc9* CRISPR-F0 fish (32).

Taken together, these results confirm that loss of *togaram1* causes ciliopathy phenotypes in zebrafish and supports a role for *togaram1* in ciliary function.

***armc9* and *togaram1* mutant zebrafish display similar phenotypes**

To further evaluate the link between *TOGARAM1* and *ARMC9*, we compared zebrafish mutants in the two genes. Following up on our previous work (32), we raised several stable (>F2) zebrafish lines harboring frameshift insertion and deletion alleles of *armc9* (Supplemental Figure 6F). Since homozygous mutants from all generated alleles have comparable phenotypes, we focused on the *armc9*^{zh505} allele for follow up experiments (Supplemental Figure 6F). This allele harbors a 110bp insertion in exon 14 that leads to exon skipping, causing a frameshift that inserts a stop codon at position 73 of exon 15. *armc9*-/- larvae have a straight body shape and an incompletely penetrant pronephric cyst phenotype affecting 44% of homozygous mutants (Figure 4A-B). In comparison, *togaram1*$^{zh509\ or\ zh510}$ mutant F2 larvae harboring frameshift mutations leading to stop codons in exons 21/22 have a slightly curved body shape and display a similar rate of kidney cysts compared to *armc9*-/- mutants (Figure 4C). Pronephric cysts and body curvature do not necessarily correlate with each other in *togaram1* mutants, as each phenotype can be found in isolation or in combination, but overall, 85 % of *togaram1*-/- larvae have at least one ciliopathy phenotype. Neither mutant displayed heart laterality defects that are seen in some zebrafish ciliopathy models. In addition to frameshift mutations in exon 21/22, we also identified a 21 bp in-frame deletion leading to loss of 7 amino acids in the TOG4 domain, of which 6 are highly conserved (*togaram1*^{zh508}, Supplemental Figure 7). Homozygous in-frame mutant larvae are indistinguishable from the frameshift mutants, suggesting that the TOG4 domain may be critical for Togaram1 function.

In addition to the pronephric cysts, both *armc9*-/- and *togaram1*-/- fish develop scoliosis as juveniles compared to wild-type (Figure 4D-F), as previously described in other zebrafish ciliary mutants (47, 48).

Given that pronephric cysts and curved bodies are typical ciliopathy phenotypes, we next analyzed the cilia in both mutants using immunofluorescence with anti-Arl13b and anti-acetylated α-tubulin antibodies. Compared to wild-type, larvae of both mutants have reduced numbers of shortened pronephric, ventricular, and nose pit cilia (Figure 4G-O), the latter being confirmed by scanning electron microscopy (Figure 4P-R). The reduced and shortened cilia in both mutants support a role for Armc9 and Togaram1 in zebrafish cilium formation and/or stability.

JBTS-associated *ARMC9* and *TOGARAM1* variants result in decreased ciliary length

To gain insight into the ciliary defects associated with JBTS in humans, we evaluated four fibroblast lines from patients with *ARMC9*-associated JBTS. Western blot analysis of total protein lysates revealed that all four cell lines express trace levels of the two major ARMC9 isoforms at 92kDa and 75.5kDa seen in control fibroblasts (32) (Figure 5A, B). To evaluate for ciliary phenotypes, we serum starved control and affected cells, and then stained with anti-acetylated α-tubulin and anti-ARL13B antibodies. All four patient lines displayed significantly shorter mean ciliary length (2.3-3.3µm, standard deviation (SD) 0.7-1.4, n = 349-1395 cilia), versus controls (3.6µm, SD 1.4, n =1395 cilia) (Figure 5C). Ciliation rates 48 hours after serum starvation were similar in the patient lines (75-86%) compared to controls (80%), suggesting that ARMC9 does not play an integral role in ciliogenesis (Figure 5D).

Mean ciliary length was also shorter the one available patient cell line from UW360-3 with *TOGARAM1*-related JBTS (2.6µm, SD 0.8, n = 154 cilia) versus control (3.0µm, SD of 1.0, n = 179 cilia) (Figure 5E). This line had a slightly lower ciliation rate than control (85% versus 91% respectively) (Figure 5F). To generate additional data about the effects of loss of TOGARAM1 function on cilia in human cells, we turned to CRISPR/Cas9 genome-edited *TOGARAM1* hTERT-RPE1 mutant cells. gRNAs targeting the translation start site of exon 1 resulted in two different lines harboring a disruption in the ATG site of both alleles of

TOGARAM1 (Supplemental Figure 5). These lines make significantly shorter cilia (mut line 1: 1.5µm, SD 0.6, n= 111 cilia; mut line 2: 1.2µm, SD 0.5, n = 178 cilia) versus the isogenic control (2.3µm, SD 0.8, n = 137 cilia) (Figure 5E). Ciliation levels in the *TOGARAM1* engineered lines (81% in mutant 1 and 69% in mutant 2) did not differ significantly from the isogenic control (67%) (Figure 5F). Taken together these results suggest that disruptions in *TOGARAM1* and *ARMC9* lead to shorter ciliary length but do not affect overall ciliation rates.

Transition zone integrity with ARMC9 and TOGARAM1 dysfunction

Given the well-described role of transition zone (TZ) dysfunction in JBTS (22), we evaluated whether the integrity of this compartment is affected by loss of TOGARAM1 or ARMC9 function. Since TZ dysfunction often results in loss of ciliary ARL13B, which secondarily causes loss of ciliary INPP5E (12, 49), we performed quantitative immunofluorescence (qIF) on control, *ARMC9*, and *TOGARAM1* patient cell lines. Our data revealed mildly lower levels of ARL13B in three of four *ARMC9* patient fibroblast lines and normal levels in the *TOGARAM1* patient fibroblast line (Figure 6A; Supplemental Figure 8A, C). Importantly, the mildly lower ARL13B levels observed in three of four ARMC9 lines were not associated with lower ciliary INPP5E (Figure 6B; Supplemental Figure 8B), indicating that the lower ARL13B levels were still sufficient to properly localize INPP5E. Western blot analysis also revealed similar levels of ARL13B and INPP5E in patient fibroblast lysates compared to control cells (Figure 6C, D). In zebrafish, Arl13b levels were not lower in either mutant (and even slightly increased in the *armc9*-/- fish) (Figure 6A, E, F). Together, these results are strikingly different from the marked ciliary ARL13B and INPP5E reduction observed in TZ mutants (12, 49). To evaluate the composition of the TZ directly, we performed immunostaining for canonical TZ proteins RPGRIP1L in human cell lines (Figure 6G, H) and Cc2d2a in zebrafish (Figure 6F). Both proteins localized normally to the TZ of the respective cilia. Taken together, these findings suggest that the TZ is generally intact, despite dysfunction of the ARMC9-TOGARAM1 complex.

TOGARAM1 dysfunction results in attenuated SMO translocation

Recent work has reported Hedgehog (Hh) signaling defects in cell lines with dysfunction of the JBTS genes *CEP104*, *CSPP1*, and *Armc9* (33, 39). Therefore, we tested whether *TOGARAM1* dysfunction leads to attenuated ciliary SMO accumulation in response to Hh stimulation in the engineered *TOGARAM1*-mutant hTERT-RPE1 cells described above (Supplemental Figure 5). We starved the cells for 24 hours to promote ciliation and then exposed them to 100 nM Smoothened agonist (SAG) for an additional 24 hours before fixation and qIF (Supplemental Figure 9A). Upon pathway stimulation, the control and two *TOGARAM1*-mutant lines exhibited a significant induction of SMO translocation into the cilium as compared to their respective DMSO treatment condition; however, the ciliary enrichment of SMO was markedly lower in the two mutant lines compared to control cells (Supplemental Figure 9B-D). Overall, SMO intensity levels in both *TOGARAM1*-mutant lines were less than 50% of the control line, and mutant lines did not differ significantly in their response when compared to each other.

ARMC9 and TOGARAM1 dysfunction affects tubulin post-translational modifications in patient fibroblasts and zebrafish mutants

During our experiments evaluating ciliary ARL13B and INPP5E, we noted that the acetylated α-tubulin and polyglutamylated tubulin signals appeared substantially less intense in patient cell lines versus controls (Figure 7A, B). Using qIF, mean acetylated tubulin levels were ~50% of control levels in the *ARMC9* lines and ~70% of controls in the *TOGARAM1* line (Figure 7E, F and Supplemental Figure 10A, B). Mean polyglutamylated signal levels were ~35% and ~45% of control levels in *ARMC9* and *TOGARAM1* lines respectively (Figure 7B, F and Supplemental Figure 10). Western blots of whole cell lysates also demonstrated substantially lower levels of both acetylated and polyglutamylated tubulin in *ARMC9* fibroblast lines compared to controls (Figure 7A, B). In the zebrafish *armc9* and *togaram1* mutant lines, we observed similar reductions of ciliary acetylated and polyglutamylated tubulin in the remaining ventricular cilia (Figure 7C-F). Together, these results indicate that loss of either ARMC9 or TOGARAM1 results in decreased post-translational modifications of axonemal tubulin across multiple model systems.

ARMC9 and TOGARAM1 dysfunction is associated with abnormal ciliary resorption

Post-translational modifications of microtubules such as acetylation and polyglutamylation are enriched in the ciliary compartment and play roles in ciliogenesis, axoneme stability, and cilium disassembly (17). To investigate the consequence of reduced ciliary microtubule post-translational modifications on axonemal stability, we evaluated cilia of control and *ARMC9* patient cells for sensitivity to cold-induced microtubule depolymerization (50, 51). In control cells, a 10-minute treatment at 4°C was not associated with reduced numbers of cilia, while cold-treated *ARMC9* patient cells had 20-30% fewer cilia than untreated cells (Figure 8A). *TOGARAM1* patient cell cilia were also more susceptible to cold-induced depolymerization, with 15% fewer cilia after treatment compared to untreated cells (Figure 8A).

As a second measure of cilium stability, we evaluated the rate of cilium resorption after serum re-addition to serum-starved cells. Serum provides growth factors that quickly initiate ciliary resorption, so that cells can re-enter the cell cycle. In controls, the ciliation rate was ~85% of baseline 4 hours after serum re-addition. In contrast, the ciliation rate was 70% of baseline in *ARMC9* patient fibroblasts only 2 hours after serum re-addition, and by 8 hours, it was down to 50%, compared to 75% in controls (Figure 8B). To determine whether the faster resorption was due to an overactive deacetylating enzyme in the *ARMC9* cell lines, we repeated these experiments with and without the histone deacetylase 6 (HDAC6) inhibitor tubacin. Tubacin treatment did not rescue the faster resorption in *ARMC9* cell lines to control levels (Supplemental Figure 11A-C). Intriguingly, the ciliation rate of the one *TOGARAM1* patient fibroblast line available remained 90% of baseline even 8 hours after serum re-addition, substantially higher than controls (Figure 8B). To determine if this abnormal ciliary stability caused defects in cell cycle progression, we used a flow-cytometry based approach to quantify cell cycle reentry (Supplemental Figure 12A-B). *ARMC9* and *TOGARAM1* patient cell lines reentered the cell cycle closely with similar timing to control cells. These data suggest that the ARMC9-TOGARAM1 complex plays a role in regulation of axonemal stability.

Discussion

In this study, we identified a new JBTS-associated protein module that can be distinguished physically and functionally from the previously described JBTS protein complex at the ciliary transition zone of primary cilia (52). Several components of this new module localize at the ciliary basal body (32) and at the proximal end of the ciliary axoneme (33, 53). Pathogenic variants in the genes encoding two directly interacting members of the module, ARMC9 and TOGARAM1, cause defects in cilium length, Hh signaling (SMO translocation), microtubule post-translational modifications (acetylation and polyglutamylation), and ciliary stability in patient-derived fibroblasts, zebrafish mutants, and genetically edited hTERT-RPE1 cell lines (Summary Figure 9).

The ARMC9-TOGARAM1 complex in JBTS

Knowledge of the components and associations of the ciliary molecular machinery has been instrumental for relating ciliopathy genetic defects, associated pathomechanisms, and the wide spectrum of overlapping ciliopathy phenotypes. Several affinity and proximity proteomics approaches have been used to determine the topology of ciliary protein-protein interaction networks and generate molecular blueprints of the ciliary machinery, e.g. the entire ciliary organelle (54), of the human centrosome-cilium interface (53), or specific ciliopathy-associated protein modules (55, 56). The majority of the previously identified JBTS-associated proteins participate in specific sub-modules of complex ciliary protein networks that vary in sub-ciliary localization, concentrating at the transition zone to organize and regulate the ciliary gate (12, 57).

Using a combination of affinity proteomics (TAP) and Y2H protein interaction screens, we found that the newly JBTS-associated protein ARMC9 interacts with known JBTS-associated proteins CSPP1 and CEP290, confirming the importance of this complex to JBTS. We also identified two ciliary microtubule-associated proteins, TOGARAM1 and CCDC66, not previously associated with JBTS. A subsequent TAP screen using TOGARAM1 as bait pulled out ARMC9, further validating their interaction, and also identified another JBTS-associated protein, CEP104 (JBTS25). By Y2H screening we determined the direct interaction of TOGARAM1 with another JBTS-associated protein, RPGRIP1L (JBTS7), while a TAP experiment using CSPP1 as a bait again identified CEP290 as a complex member, and confirmed its previously identified interaction with RPGRIP1L (58). Our results are in agreement with the BioID proximity interactome of CEP104 that contained most of our module components, except for ARMC9 and RPGRIP1L (53). Co-IP and yeast two-hybrid analysis validated the core module, ARMC9, TOGARAM1, CCDC66, and CEP104 consisting of proteins important for cilium function and ciliopathy disease. For instance, CCDC66 was previously found to interact with CEP290 (36) and null mutations cause retinal degeneration in dogs (59) and mice (60). CEP104 localizes both to the daughter centriole as well as to the apical tip of a growing cilium (30) and, similar to TOGARAM1, interacts with tubulin through its TOG domain (61). Moreover, CEP104 has been shown to interact with NEK1 (61), which is associated with the ciliopathy “short-rib polydactyly syndrome Majewski type” (62), and with the JBTS-associated protein CSPP1 (39). This interaction, that we confirmed in our co-IP experiments, is required for the formation of Hedgehog signaling-competent cilia, as mutations in CSPP1 and CEP104 significantly decreased ciliary SMO translocation (39), similar to what we observed with RPE1 *TOGARAM1* mutant lines. Following the “guilt by association” paradigm, we next found biallelic *TOGARAM1* variants in multiple individuals with JBTS, reiterating the relevance of the complex to JBTS, and moving us closer to identifying all genetic causes of this disorder. We did not find *CCDC66* variants in >600 families affected by JBTS, indicating that variants in this gene are, at most, a very rare cause of JBTS.

Role of the ARMC9-TOGARAM1 complex in ciliary length and stability

The structure of TOG domains is highly conserved for microtubule binding, where the intra-HEAT loop in the discontinuous TOG domain binds tubulin (63–66). TOG domains are thought to regulate microtubule growth and dynamics (67). The TOG domains in TOGARAM1 have differential microtubule binding capacity and likely function in concert to coordinate microtubule polymerization (34). For example, the C-terminal TOG domains TOG3 and TOG4 promote microtubule lattice binding (34). Interestingly, we found that cilia are shorter in cells with *ARMC9* or *TOGARAM1* dysfunction. In contrast, we demonstrate that TOGARAM1 overexpression results in long cilia, and this effect requires an intact TOG3 domain, but not an intact TOG2 domain which is required for TOGARAM1 interaction with ARMC9. In fact, the TOG3 domain Arg1311Cys variant does not interfere with the ARMC9 interaction, but over-expression of this mutant protein results in severely shortened cilia. Since both long and short cilia have been identified in fibroblasts from patients with different genetic causes of JBTS, no simple correlation between cilium length and JBTS disease mechanism can be made (31, 32, 68, 69).

Recent work in *Tetrahymena* indicates that *TOGARAM1* and *ARMC9* orthologs may have opposite effects on B-tubule length (29). In mammalian cells, we found that dysfunction of either gene leads to shorter cilia, decreased post-translational modifications, and sensitivity to cold-induced ciliary microtubule depolymerization, suggesting reduced ciliary stability. Intriguingly, TOGARAM1 and ARMC9 dysfunction seem to have opposite effects on the kinetics of cilium resorption after serum re-addition in patient fibroblasts. This result suggests that different mechanisms may underlie ciliary resorption in the setting of serum re-addition versus cold-induced depolymerization. The latter may represent an acute stressor directly correlated with cilium stability, while the former is a regulated mechanism required for cell cycle reentry, for which TOGARAM1 and ARMC9 may indeed play opposing roles as suggested by the work in *Tetrahymena* (29).

Post-translational modifications of ciliary microtubules

ARMC9 and *TOGARAM1* dysfunction also leads to significantly decreased axonemal post-translational modifications (PTMs, polyglutamylation and acetylation) in patient fibroblasts and zebrafish, supporting the relevance of altered PTMs in JBTS. Tubulin PTMs are indispensable for proper microtubule function, affecting their mechanical properties, stability, and binding of microtubule-associated proteins (MAPs) to influence protein trafficking and signaling (17).

Polyglutamylation decorates the surface of axonemal microtubules. This reversible modification ranges from 1-17 glutamyl residues *in vivo* (70), and plays a role in intraflagellar transport activity and MAP binding (71–74). Decreased ciliary polyglutamylation interferes with kinesin2-mediated anterograde transport, also on the B-tubule, and subsequently negatively impacts Hedgehog signaling (72, 73). Some MAPs are sensitive to the amount of glutamylation. For example, spastin has optimal microtubule-severing activity *in vitro* with moderate polyglutamylation, while both hypo- and hyper-glutamylation suppresses severing activity (75). In the context of JBTS, decreased axonemal polyglutamylation was reported in fibroblasts from patients with *CEP41*-related JBTS (11). More recent work found decreased axonemal glutamylation with *ARL13B*, *FIP5* and *TTLL5* knockdown in immortalized cells, associated with impacts on polycystin localization and Hh signaling (71).

While most PTMs are added to the C-terminus of tubulin on the microtubular surface, acetylation uniquely occurs on the luminal surface of α-tubulin. Ciliary resorption requires removal of this modification by HDAC6 (76). It has been long observed that the hyperstabilized ciliary microtubules are acetylated, but until recently it was not known if the modification confers stability or if long-lived stable microtubules accumulate this modification. Recent work using cryo-EM confirmed that acetylation causes a stabilizing conformational change (77). This is in line with our findings of decreased axonemal microtubule acetylation and stability with ARMC9 and TOGARAM1 dysfunction, as well as previously published findings with *Kif7* and *Armc9* dysfunction (33, 68). In particular, *Armc9* null NIH3T3 cells had short cilia and decreased acetylation and glutamylation. The more rapid ciliary resorption with ARMC9 dysfunction is unlikely due to excessive deacetylation since cilia were not stabilized by HDAC6 inhibition. Interestingly, *Kif7* mutant mouse embryonic fibroblasts (MEFs) exhibited reduced glutamylation, making it the only other JBTS model with decreases in both of these PTMs (31, 68). Fibroblasts from patients with *INPP5E*-related JBTS also display decreased cilium stability (78). Notably, these models of *KIF7*- and *INPP5E*-related ciliary dysfunction disrupt Hh signaling, likely due to GLI/SUFU mislocalization and aberrant phosphatidylinositol composition respectively, while emerging evidence indicates that reduced polyglutamlyation may indirectly alter translocation of Hh pathway components by perturbing anterograde intraflagellar transport (71, 72).

The observed reduction of PTMs with *ARMC9* and *TOGARAM1* dysfunction could therefore affect ciliary function through loss of stability and/or direct disruption of signaling pathways. In fact, *Armc9* and *Togaram1* (FAM179B) were identified as positive regulators of the Hh pathway in a genome-wide screen for Hh signaling components (33). That study also demonstrated that over-expressed ARMC9 translocates from the ciliary base to the tip upon Hh pathway stimulation (33). In *Tetrahymena*, orthologs of ARMC9 and TOGARAM1 are seen at both the base and tip, with tip enrichment during cilia regeneration (29).

Taken together, these results suggest a dynamic localization of the complex members, and likely changes in protein complex composition at each locale. Further work will be required to determine the details of dynamic ARMC9-TOGARAM1 localization during ciliogenesis, resorption, and signaling.

Conclusions

The biological mechanisms underlying JBTS remain incompletely understood. This work brings us one step closer to the complete catalog of JBTS genetic causes, and highlights the role of a new JBTS-associated protein complex including ARMC9 and TOGARAM1. Approximately half of JBTS-associated genes are implicated in transition zone function which is required for ciliary ARL13B and INPP5E localization. In contrast, the ARMC9-TOGARAM1 complex is not required for INPP5E localization, and instead, appears to regulate the post-translational modification of ciliary microtubules, ciliary length and ciliary stability. Future work will need to reconcile how the diverse array of cellular defects associated with loss of function for the JBTS genes relate to this important human disorder.

Materials and Methods

A detailed description of cell culturing conditions, cloning, immunofluorescence and microscopy, cell cycle assay, zebrafish experiments, Palm-Myr assay, tandem affinity purification, yeast two-hybrid interaction analysis, coimmunoprecipitation, statistical analysis, microtubule cold assay, cilia stability assay, subject ascertainment and phenotypic data, variant identification, and array CGH can be found in the supplemental material and methods file.

Web resources

http://chopchop.cbu.uib.no

http://gnomad.broadinstitute.org

https://www.ensembl.org/index.html

http://www.cmbi.umcn.nl/hope/

https://huygens.science.uva.nl/PlotsOfData/ (79)

http://www.phylogeny.fr/

http://syntenydb.uoregon.edu/synteny_db/

Acknowledgements

We thank the patient and parents for their participation in this research. We thank Dr David Breslow (Yale University) and Dr Max Nachury (University of California San Francisco) for providing the ARMC9-3xFlag IMCD3 FlpIn lines and NIH-3T3 ARMC9 mutant lines. The research leading to these results has received funding from the Netherlands Organisation for Scientific Research (NWO Vici-865.12.005 to R.R.), the Netherlands Organisation for Health Research and Development (ZonMW, #91216051 to R.R.), the Foundation Fighting Blindness (PPA-0717-0719-RAD to M.U. and R.R.), the Tistou & Charlotte Kerstan

Stiftung (to M.U.), the Swiss National Science Foundation SNF (PP00P3_170681 to R.B.G and 31003A_173083 to S.C.F.N.), the Zurich Neuroscience Center (to R.B.G), the NIH Eunice Kennedy Shriver National Institute of Child Health and Human Development (U54HD083091 Genetics Core and sub-project 6849 to D.D. and F32 HD095599 to J.V.D.W.), private donations (to D.D.), Watson Genetic Laboratory (Tehran, Iran) for WGL-1914 sequencing (to M.K.), NIH National Human Genome Research Institute (U54HG006493 to M.B. and D.N.), Kidney Research UK, the Northern Counties Kidney Research Fund (joint studentship ST_001_20171120 to M.B.-G. and 18/01 to J.A.S.), and the King Salman Center for Disability Research (FSA). Part of the data presented here was provided through access to the data and findings generated by the 100,000 Genomes Project, which is funded by the NIHR and NHS England.

Author contributions

R.B.-G., R.R. and D.D. conceived the overall project. B.L., J.V.D.W., T.D.S.R., J.C.D., S.C.F.N., K.B., M.U., M.K., J.A.S., F.S.A., R.B.-G., R.R., & D.D. designed experiments and led the data generation and processing. B.L., J.V.D.W., T.D.S.R., S.J.F.L., A.G., A.K., M.A, M.E.G., S.E.C.v.B., C.V.M., and U.W.C.M.G. performed experiments. R.S., M.C., H.M., & J.C.D acquired clinical phenotype data. B.L., J.V.D.W., T.D.S.R., M.G., M.E.G., C.M., R.B.-G., R.R., & D.D. analyzed and interpreted data. B.L., J.V.D.W., T.D.S.R., R.B.-G., R.R., & D.D. wrote the paper with input from all authors.

References

1. Hildebrandt F, Benzing T, Katsanis N. Ciliopathies. *N. Engl. J. Med.* 2011;364(16):1533–1543.

2. van Reeuwijk J, Arts HH, Roepman R. Scrutinizing ciliopathies by unraveling ciliary interaction networks. *Hum. Mol. Genet.* 2011;20(R2):R149–57.

3. Satir P, Pedersen LB, Christensen ST. The primary cilium at a glance. *J. Cell Sci.* 2010;123(Pt 4):499–503.

4. Maria BL et al. "Joubert Syndrome" Revisited: Key Ocular Motor Signs With Magnetic Resonance Imaging Correlation. *J. Child Neurol.* 2016;12(7):423–430.

5. Sattar S, Gleeson JG. The ciliopathies in neuronal development: a clinical approach to investigation of Joubert syndrome and Joubert syndrome-related disorders. *Dev. Med. Child Neurol.* 2011;53(9):793–798.

6. Reiter JF, Leroux MR. Genes and molecular pathways underpinning ciliopathies. *Nat. Rev. Mol. Cell Biol.* 2017;18(9):533–547.

7. Shamseldin HE et al. The morbid genome of ciliopathies: an update. *Genet. Med.* 2020;1–10.

8. Bachmann-Gagescu R et al. Healthcare recommendations for Joubert syndrome. *Am. J. Med. Genet. Part A* 2019;182(1):229–249.

9. Chaki M et al. Exome capture reveals ZNF423 and CEP164 mutations, linking renal ciliopathies to DNA damage response signaling. *Cell* 2012;150(3):533–548.

10. Bielas SL et al. Mutations in INPP5E, encoding inositol polyphosphate-5-phosphatase E, link phosphatidyl inositol signaling to the ciliopathies. *Nat. Genet.* 2009;41(9):1032–1036.

11. Lee JE et al. CEP41 is mutated in Joubert syndrome and is required for tubulin glutamylation at the cilium. *Nat. Genet.* 2012;44(2):193–199.

12. Garcia-Gonzalo FR et al. A transition zone complex regulates mammalian ciliogenesis and ciliary membrane composition. *Nat. Genet.* 2011;43(8):776–784.

13. Valente EM et al. Mutations in TMEM216 perturb ciliogenesis and cause Joubert, Meckel and related syndromes. *Nat. Genet.* 2010;42(7):619–625.

14. Garcia-Gonzalo FR et al. Phosphoinositides Regulate Ciliary Protein Trafficking to Modulate Hedgehog Signaling. *Dev. Cell* 2015;34(4):400–409.

15. Piperno G, Fuller MT. Monoclonal antibodies specific for an acetylated form of alpha-tubulin recognize the antigen in cilia and flagella from a variety of organisms. *J. Cell Biol.* 1985;101(6):2085–2094.

16. Bré MH, de Néchaud B, Wolff A, Fleury A. Glutamylated tubulin probed in ciliates with the monoclonal antibody GT335. *Cell Motil. Cytoskeleton* 2005;27(4):337–349.

17. Wloga D, Joachimiak E, Louka P, Gaertig J. Posttranslational Modifications of Tubulin and Cilia. *Cold Spring Harb. Perspect. Biol.* 2017;9(6):a028159–16.

18. Arts HH et al. Mutations in the gene encoding the basal body protein RPGRIP1L, a nephrocystin-4 interactor, cause Joubert syndrome. *Nat. Genet.* 2007;39(7):882–888.

19. Delous M et al. The ciliary gene RPGRIP1L is mutated in cerebello-oculo-renal syndrome (Joubert syndrome type B) and Meckel syndrome. *Nat. Genet.* 2007;39(7):875–881.

20. Gorden NT et al. CC2D2A is mutated in Joubert syndrome and interacts with the ciliopathy-associated basal body protein CEP290. *Am. J. Hum. Genet.* 2008;83(5):559–571.

21. Williams CL et al. MKS and NPHP modules cooperate to establish basal body/transition zone

membrane associations and ciliary gate function during ciliogenesis. *J. Cell Biol.* 2011;192(6):1023–1041.

22. Shi X et al. Super-resolution microscopy reveals that disruption of ciliary transition-zone architecture causes Joubert syndrome. *Nat. Cell Biol.* 2017;19(10):1178–1188.

23. Cantagrel V et al. Mutations in the Cilia Gene ARL13B Lead to the Classical Form of Joubert Syndrome. *Am. J. Hum. Genet.* 2008;83(2):170–179.

24. Chávez M et al. Modulation of Ciliary Phosphoinositide Content Regulates Trafficking and Sonic Hedgehog Signaling Output. *Dev. Cell* 2015;34(3):338–350.

25. Caspary T, Larkins CE, Anderson K V. The Graded Response to Sonic Hedgehog Depends on Cilia Architecture. *Dev. Cell* 2007;12(5):767–778.

26. Tuz K et al. Mutations in CSPP1 cause primary cilia abnormalities and Joubert syndrome with or without Jeune asphyxiating thoracic dystrophy. *Am. J. Hum. Genet.* 2014;94(1):62–72.

27. Shaheen R et al. Mutations in CSPP1, Encoding a Core Centrosomal Protein, Cause a Range of Ciliopathy Phenotypes in Humans. *Am. J. Hum. Genet.* 2014;94(1):73–79.

28. Srour M et al. Joubert Syndrome in French Canadians and Identification of Mutations in CEP104. *Am. J. Hum. Genet.* 2015;97(5):744–753.

29. Louka P et al. Proteins that control the geometry of microtubules at the ends of cilia. *J. Cell Biol.* 2018;217(12):4298–4313.

30. Satish Tammana T V, Tammana D, Diener DR, Rosenbaum J. Centrosomal protein CEP104 (Chlamydomonas FAP256) moves to the ciliary tip during ciliary assembly. *J. Cell Sci.* 2013;126(21):5018–5029.

31. Dafinger C et al. Mutations in KIF7 link Joubert syndrome with Sonic Hedgehog signaling and microtubule dynamics. *J. Clin. Invest.* 2011;121(7):2662–2667.

32. Van De Weghe JC et al. Mutations in ARMC9, which Encodes a Basal Body Protein, Cause Joubert Syndrome in Humans and Ciliopathy Phenotypes in Zebrafish. *Am. J. Hum. Genet.* 2017;101(1).

33. Breslow DK et al. A CRISPR-based screen for Hedgehog signaling provides insights into ciliary function and ciliopathies. *Nat. Genet.* 2018;50(3):460–471.

34. Das A, Dickinson DJ, Wood CC, Goldstein B, Slep KC. Crescerin uses a TOG domain array to regulate microtubules in the primary cilium. *Mol. Biol. Cell* 2015;26(23):4248–4264.

35. Jiang K et al. A Proteome-wide Screen for Mammalian SxIP Motif-Containing Microtubule Plus-End Tracking Proteins. *Curr. Biol.* 2012;22(19):1800–1807.

36. Conkar D et al. The centriolar satellite protein CCDC66 interacts with CEP290 and functions in cilium formation and trafficking. *J. Cell Sci.* 2017;130(8):1450–1462.

37. Letteboer SJF, Roepman R. Versatile screening for binary protein-protein interactions by yeast two-hybrid mating. *Methods Mol. Biol.* 2008;484:145–159.

38. Conkar D, Bayraktar H, Firat-Karalar EN. Centrosomal and ciliary targeting of CCDC66 requires cooperative action of centriolar satellites, microtubules and molecular motors. *Sci. Rep.* 2019;9(1):14217–14250.

39. Frikstad K-AM et al. A CEP104-CSPP1 Complex Is Required for Formation of Primary Cilia Competent in Hedgehog Signaling. *Cell Rep.* 2019;28(7):1907–1922.e6.

40. Zacharias DA, Violin JD, Newton AC, Tsien RY. Partitioning of lipid-modified monomeric GFPs into membrane microdomains of live cells. *Science.* 2002;296(5569):913–916.

41. Bachmann-Gagescu R et al. Joubert syndrome: a model for untangling recessive disorders with extreme genetic heterogeneity. *J. Med. Genet.* 2015;52(8):514–522.

42. Karczewski KJ et al. Variation across 141,456 human exomes and genomes reveals the spectrum of loss-of-function intolerance across human protein-coding genes [Preprint]. https://doi.org/10.1101/531210. Posted on *bioRxiv* August 13, 2019.

43. Rentzsch P, Witten D, Cooper GM, Shendure J, Kircher M. CADD: predicting the deleteriousness of variants throughout the human genome. *Nucleic Acids Res.* 2018;47(D1):D886–D894.

44. O'Roak BJ et al. Exome sequencing in sporadic autism spectrum disorders identifies severe de novo mutations. *Nat. Genet.* 2011;43(6):585–589.

45. Venselaar H, Te Beek TAH, Kuipers RKP, Hekkelman ML, Vriend G. Protein structure analysis of mutations causing inheritable diseases. An e-Science approach with life scientist friendly interfaces. *BMC Bioinformatics* 2010;11:548.

46. Nithianantham S et al. Structural basis of tubulin recruitment and assembly by microtubule polymerases with tumor overexpressed gene (TOG) domain arrays. *Elife* 2018;7:1–60.

47. Grimes DT et al. Zebrafish models of idiopathic scoliosis link cerebrospinal fluid flow defects to spine curvature. *Science.* 2016;352(6291):1341–1344.

48. Bachmann-Gagescu R et al. The ciliopathy gene cc2d2a controls zebrafish photoreceptor outer segment development through a role in Rab8-dependent vesicle trafficking. *Hum. Mol. Genet.* 2011;20(20):4041–4055.

49. Slaats GG et al. MKS1 regulates ciliary INPP5E levels in Joubert syndrome. *J. Med. Genet.* 2015;53(1):62–72.

50. Piperno G, LeDizet M, Chang XJ. Microtubules containing acetylated alpha-tubulin in mammalian cells in culture. *J. Cell Biol.* 1987;104(2):289–302.

51. LeDizet M, Piperno G. Cytoplasmic microtubules containing acetylated alpha-tubulin in Chlamydomonas reinhardtii: spatial arrangement and properties. *J. Cell Biol.* 1986;103(1):13–22.

52. Reiter JF, Blacque OE, Leroux MR. The base of the cilium: roles for transition fibres and the transition zone in ciliary formation, maintenance and compartmentalization. *EMBO Rep.* 2012;13(7):608–618.

53. Gupta GD et al. A Dynamic Protein Interaction Landscape of the Human Centrosome-Cilium Interface. *Cell* 2015;163(6):1484–1499.

54. Boldt K et al. An organelle-specific protein landscape identifies novel diseases and molecular mechanisms. *Nat. Commun.* 2016;7:1–13.

55. Toriyama M et al. The ciliopathy-associated CPLANE proteins direct basal body recruitment of intraflagellar transport machinery. *Nat. Genet.* 2016;48(6):648–656.

56. Sang L et al. Mapping the NPHP-JBTS-MKS Protein Network Reveals Ciliopathy Disease Genes and Pathways. *Cell* 2011;145(4):513–528.

57. Garcia-Gonzalo FR, Reiter JF. Scoring a backstage pass: Mechanisms of ciliogenesis and ciliary access. *J. Cell Biol.* 2012;197(6):697–709.

58. Patzke S et al. CSPP is a ciliary protein interacting with Nephrocystin 8 and required for cilia formation. *Mol. Biol. Cell* 2010;21(15):2555–2567.

59. Dekomien G et al. Progressive retinal atrophy in Schapendoes dogs: mutation of the newly identified CCDC66 gene. *Neurogenetics* 2009;11(2):163–174.

60. Gerding WM et al. Ccdc66 null mutation causes retinal degeneration and dysfunction. *Hum. Mol.*

Genet. 2011;20(18):3620–3631.

61. Al-Jassar C et al. The Ciliopathy-Associated Cep104 Protein Interacts with Tubulin and Nek1 Kinase. *Structure* 2017;25(1):146–156.

62. Thiel C et al. NEK1 mutations cause short-rib polydactyly syndrome type majewski. *Am. J. Hum. Genet.* 2011;88(1):106–114.

63. Howard AE, Fox JC, Slep KC. Drosophila melanogaster mini spindles TOG3 utilizes unique structural elements to promote domain stability and maintain a TOG1- and TOG2-like tubulin-binding surface. *J. Biol. Chem.* 2015;290(16):10149–10162.

64. Leano JB, Rogers SL, Slep KC. A cryptic TOG domain with a distinct architecture underlies CLASP-dependent bipolar spindle formation. *Structure* 2013;21(6):939–950.

65. Slep KC. A Cytoskeletal Symphony: Owed to TOG. *Dev. Cell* 2018;46(1):5–7.

66. Al-Bassam J et al. CLASP promotes microtubule rescue by recruiting tubulin dimers to the microtubule. *Dev. Cell* 2010;19(2):245–258.

67. Leano JB, Slep KC. Structures of TOG1 and TOG2 from the human microtubule dynamics regulator CLASP1. *PLoS One* 2019;14(7).

68. He M et al. The kinesin-4 protein Kif7 regulates mammalian Hedgehog signalling by organizing the cilium tip compartment. *Nat. Cell Biol.* 2014;16(7):663–672.

69. Srivastava S et al. A human patient-derived cellular model of Joubert syndrome reveals ciliary defects which can be rescued with targeted therapies. *Hum. Mol. Genet.* 2017;26(23):4657–4667.

70. Geimer S, Teltenkötter A, Plessmann U, Weber K, Lechtreck KF. Purification and characterization of basal apparatuses from a flagellate green alga. *Cell Motil. Cytoskeleton* 1997;37(1):72–85.

71. He K et al. Axoneme polyglutamylation regulated by Joubert syndrome protein ARL13B controls ciliary targeting of signaling molecules. *Nat. Commun.* 2018;9(1):3310–3314.

72. Hong S-R et al. Spatiotemporal manipulation of ciliary glutamylation reveals its roles in intraciliary trafficking and Hedgehog signaling. *Nat. Commun.* 2018;9(1):1713–1732.

73. OHagan R et al. Glutamylation Regulates Transport, Specializes Function, and Sculpts the Structure of Cilia. *Curr. Biol.* 2017;27(22):3430–3441.e6.

74. Orbach R, Howard J. The dynamic and structural properties of axonemal tubulins support the high length stability of cilia. *Nat. Commun.* 2019;1–11.

75. Valenstein ML, Roll-Mecak A. Graded Control of Microtubule Severing by Tubulin Glutamylation. *Cell* 2016;164(5):911–921.

76. Pugacheva EN, Jablonski SA, Hartman TR, Henske EP, Golemis EA. HEF1-Dependent Aurora A Activation Induces Disassembly of the Primary Cilium. *Cell* 2007;129(7):1351–1363.

77. Eshun-Wilson L et al. Effects of α-tubulin acetylation on microtubule structure and stability. *Proc. Natl. Acad. Sci. U. S. A.* 2019;116(21):10366–10371.

78. Hardee I et al. Defective ciliogenesis in INPP5E-related Joubert syndrome. *Am. J. Med. Genet. Part A* 2017;173(12):3231–3237.

79. Postma M, Goedhart J. PlotsOfDataA web app for visualizing data together with their summaries. *PLoS Biol.* 2019;17(3):e3000202–8.

Figure Legends

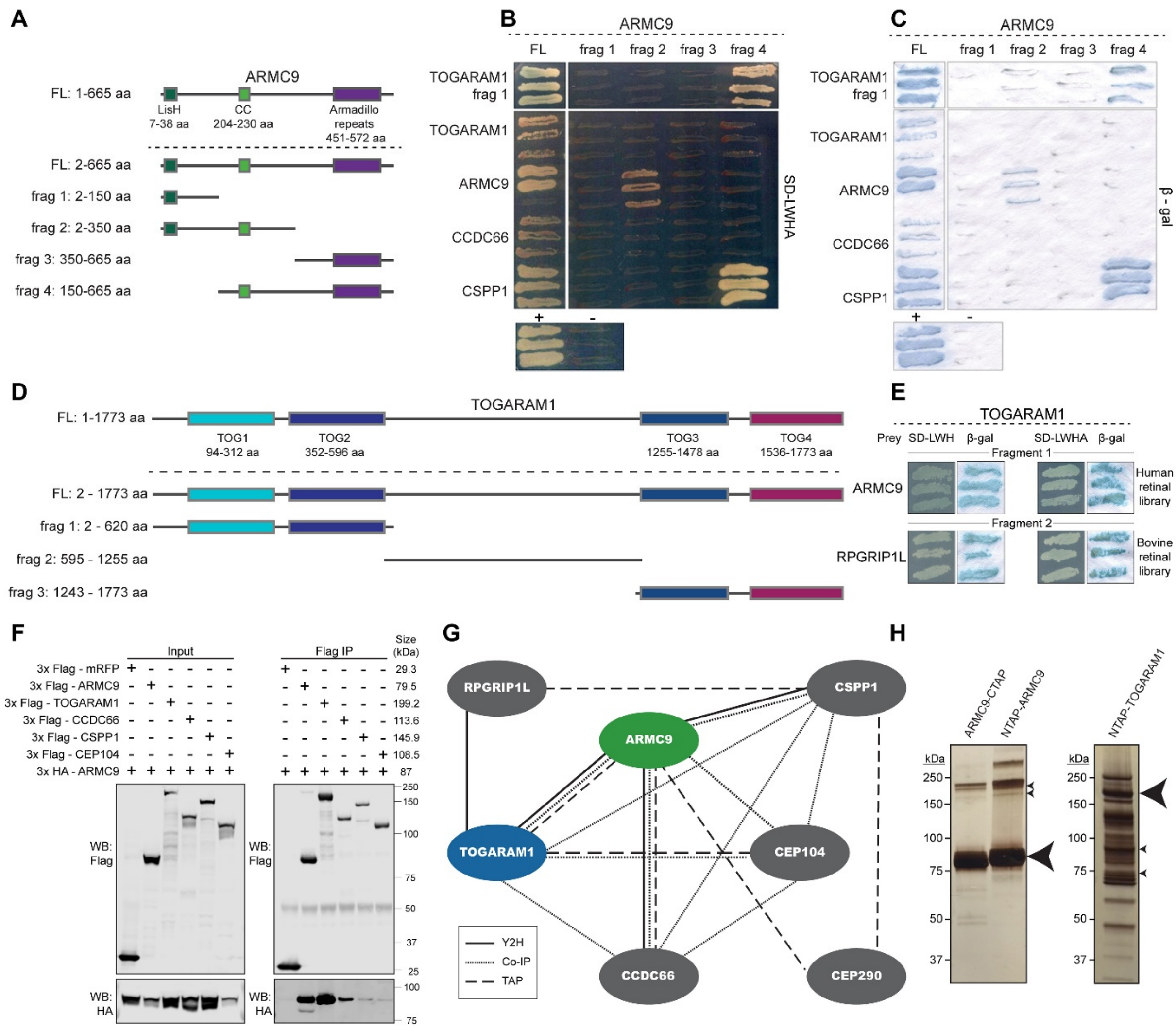

Figure 1 ARMC9 associates with TOGARAM1 in a ciliary module. **(A)** Schematic of full-length ARMC9 and fragments used as baits in Y2H bovine and human retinal cDNA library screens. Domains indicated are the predicted Lissencephaly type-1-like homology motif (LisH, dark green), coiled-coil domain (CC, light green) and the armadillo repeats-containing domain (armadillo, purple). **(B)** Direct interaction analysis grid using full length prey constructs. Selection of strains co-expressing bait and prey constructs was performed on quadruple knockout SD medium (SD-LWHA). The top row displays yeast colony growth when using fragment 1 of TOGARAM1 as prey. **(C)** β-Galactosidase activity assay confirming the interactions. **(D)**

Schematic of full-length TOGARAM1 and fragments used in Y2H bovine and human retinal cDNA screens. **(E)** TOGARAM1 screen results validated in a Y2H directed interaction analysis on triple (SD-LWH) and quadruple (SD-LWHA) knockout media. **(F)** Flag co-IP of 3xFlag-ARMC9, 3xFlag-TOGARAM1, 3xFlag-CCDC66, 3xFlag-CSPP1, and 3xFlag-CEP104 with 3xHA-ARMC9. 3xFlag-mRFP served as a negative control. Western blot analysis post Flag-tag purification indicates the presence of 3xHA-ARMC9 confirming the interactions. 3xFlag-mRFP shows no interaction with 3xHA-ARMC9. **(G)** ARMC9 interacts with TOGARAM1 as confirmed by TAP, dashed lines, and Y2H screens, solid lines. Validation was subsequently performed using co-IP, dotted lines. **(H)** Silver stain gel of C-terminally and N-terminally SF-TAP tagged ARMC9 (left, large arrow, 80 kDa) and N-terminally SF-TAP tagged TOGARAM1 (right, large arrow, 200 kDa) post protein purification. The small arrows indicate the expected protein bands of two TOGARAM1 isoforms (195.6 kDa and 189.4 kDa) in the ARMC9 TAP purification, and two endogenous ARMC9 isoforms (91.8 kDa and 75.7 kDa) in the TOGARAM1 TAP purification.

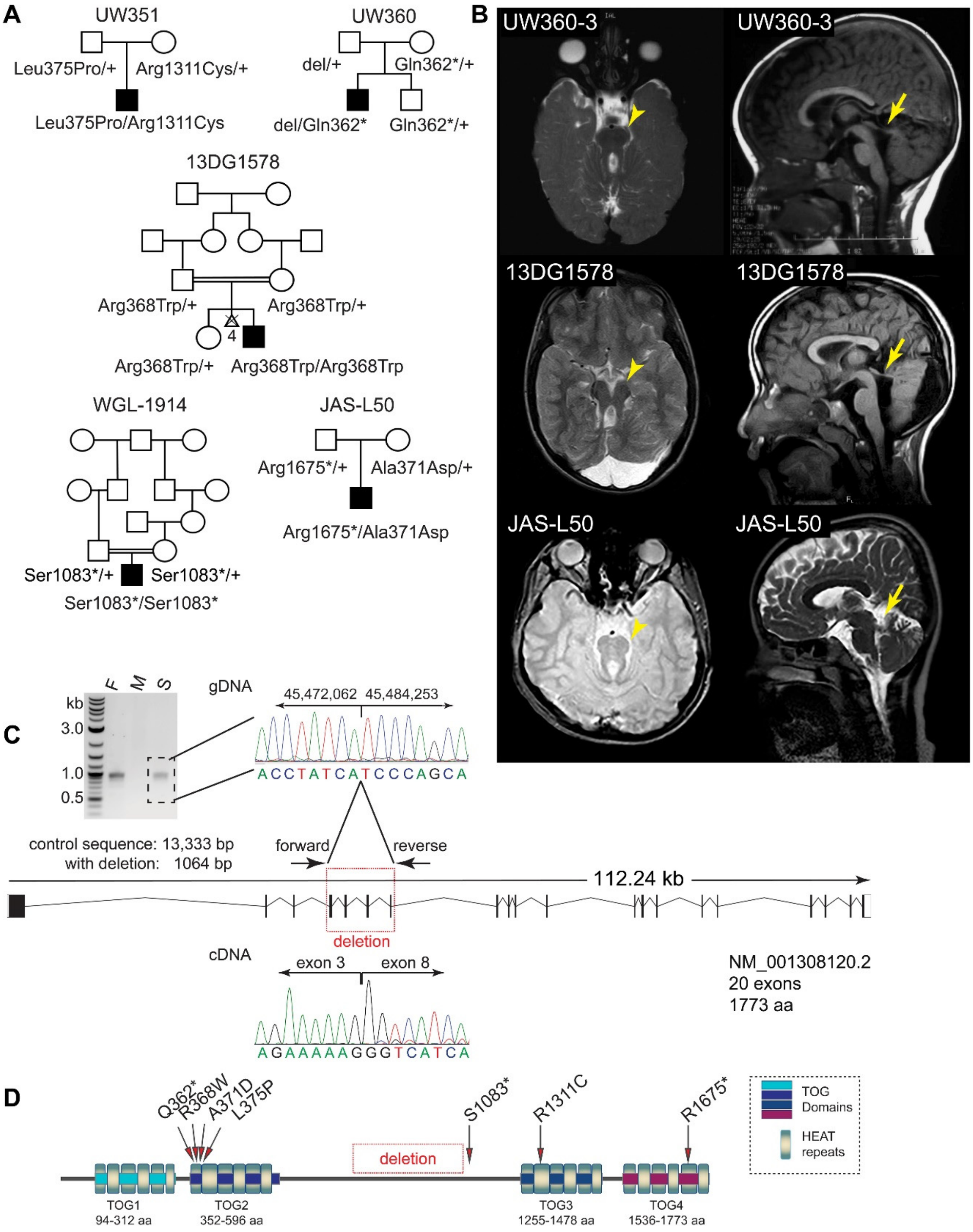

Figure 2 *TOGARAM1* variants cause JBTS. **(A)** Pedigrees and segregation of *TOGARAM1* variants**. (B)** Brain imaging features in individuals with *TOGARAM1*-related JBTS. Molar tooth sign (arrowheads in left column, axial T2-weighted images), and elevated roof of the 4th ventricle (arrows in right column, sagittal

T1-weighted (top two) and T2-weighted (bottom) images). Much of the cerebellar tissue on the sagittal images (right column) is hemisphere based on axial and coronal views (not shown). **(C)** Multi-exon deletion in UW360. Primers flanking the predicted deletion amplify a 1064 base pair product in father (F) and affected son (S) due to a 12,191 base pair deletion, but not mother (M) because the predicted product is too large. Sanger sequencing of the breakpoint in gDNA (upper) and cDNA (lower) from the affected child, confirming deletion of exons 4-7. Coding genomic schematic of *Homo sapiens* TOG array regulator of axonemal microtubules 1, *TOGARAM1*. Transcript variant 1 is shown (NM_001308120, variant 2 NM_015091.2, not shown). **(D)** Protein schematic of TOGARAM1 with JBTS associated variants indicated, TOG domains 1-4 are shown with HEAT repeats indicated in gradient blue.

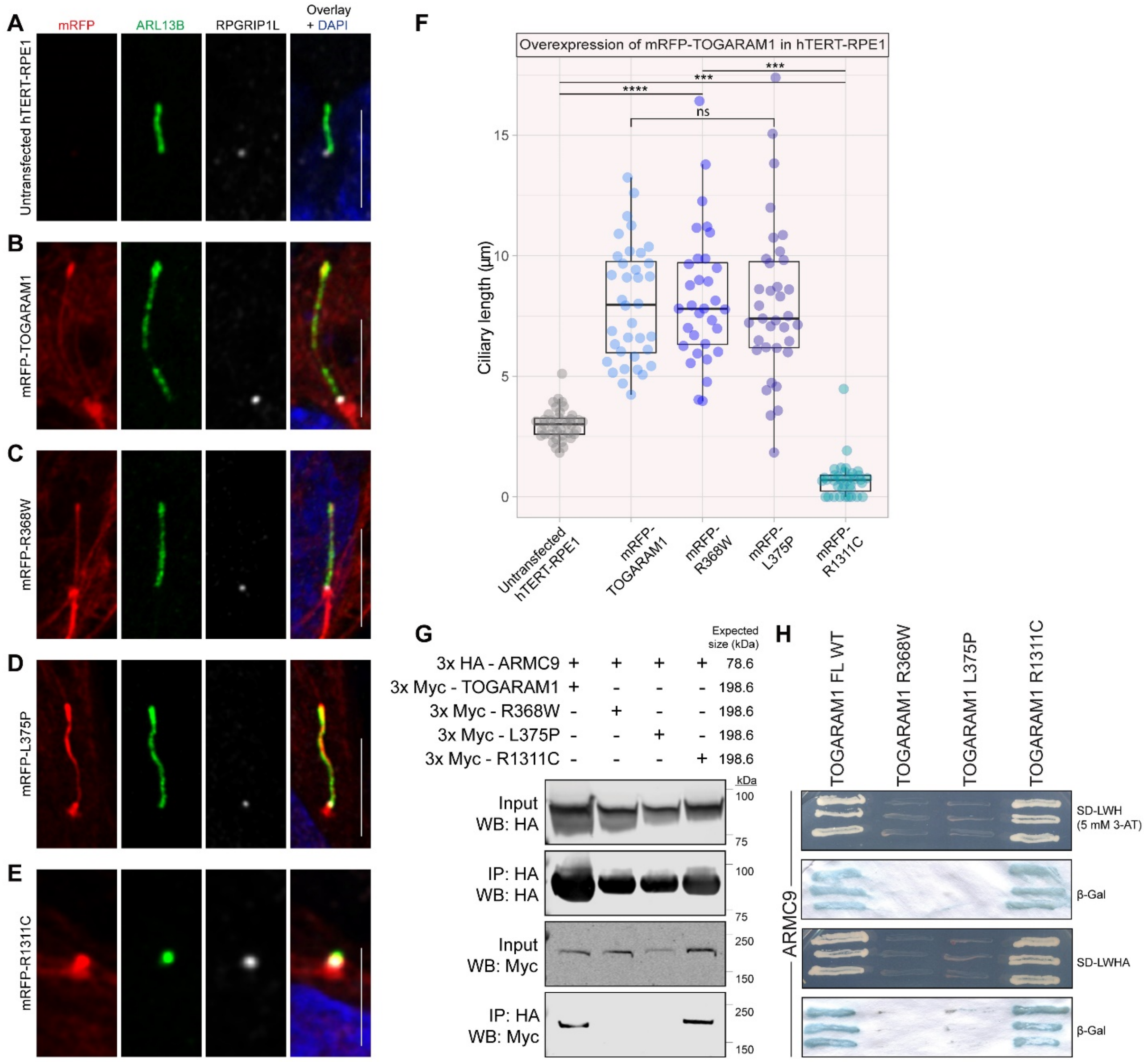

Figure 3 Overexpression of TOGARAM1 affects ciliary length and TOG2 domain variants reduce ARMC9 interaction. **(A)** Untransfected control hTERT-RPE1 cells, the cilium is shown with transition zone marker RPGRIP1L (white) and ciliary membrane marker ARL13B (green). **(B-E)** Transient mRFP-TOGARAM1 overexpression (red) in hTERT-RPE1 cells shown with transition zone marker RPGRIP1L (white) and ciliary membrane marker ARL13B (green): **(B)** mRFP-TOGARAM1-wild-type, **(C)** mRFP-TOGARAM1-Arg368Trp, **(D)** mRFP-TOGARAM1-Leu375Pro, and **(E)** mRFP-TOGARAM1-Arg1311Cys. Images are representative of >30 cilia assessed per condition over three experiments. Scale bars are 5µm. **(F)** Quantification of cilium

lengths with overexpression of wild-type and variant forms of mRFP-TOGARAM1. (untransfected n=39, wild-type n=36, Arg368Trp n=32, Leu375Pro n=35, Arg1311Cys n=36). Box plot horizontal bars represent the median +/- 95CI. Significance was tested by one-way ANOVA and Tukey's multiple comparison test. No significant differences were found between cells overexpressing mRFP-TOGARAM1, mRFP-Arg368Trp, and mRFP-Leu375Pro. p=0.0004 for untransfected versus Arg1311Cys **(G)** Co-immunoprecipitation of HA-tagged ARMC9 and Myc-tagged TOGARAM1: Wild-type and Myc-tagged TOGARAM1-Arg1311Cys interact with ARMC9, while TOGARAM1 variants Arg368Trp and Leu375Pro do not. **(H)** Y2H direct interaction analysis assay with ARMC9 and TOGARAM1: Wild-type and TOGARAM1-Arg1311Cys interact with ARMC9 while the TOGARAM1 variants Arg368Trp and Leu375Pro do not. P-value symbols: ns $p>0.05$, ***$p \leq 0.001$, ****$p \leq 0.0001$.

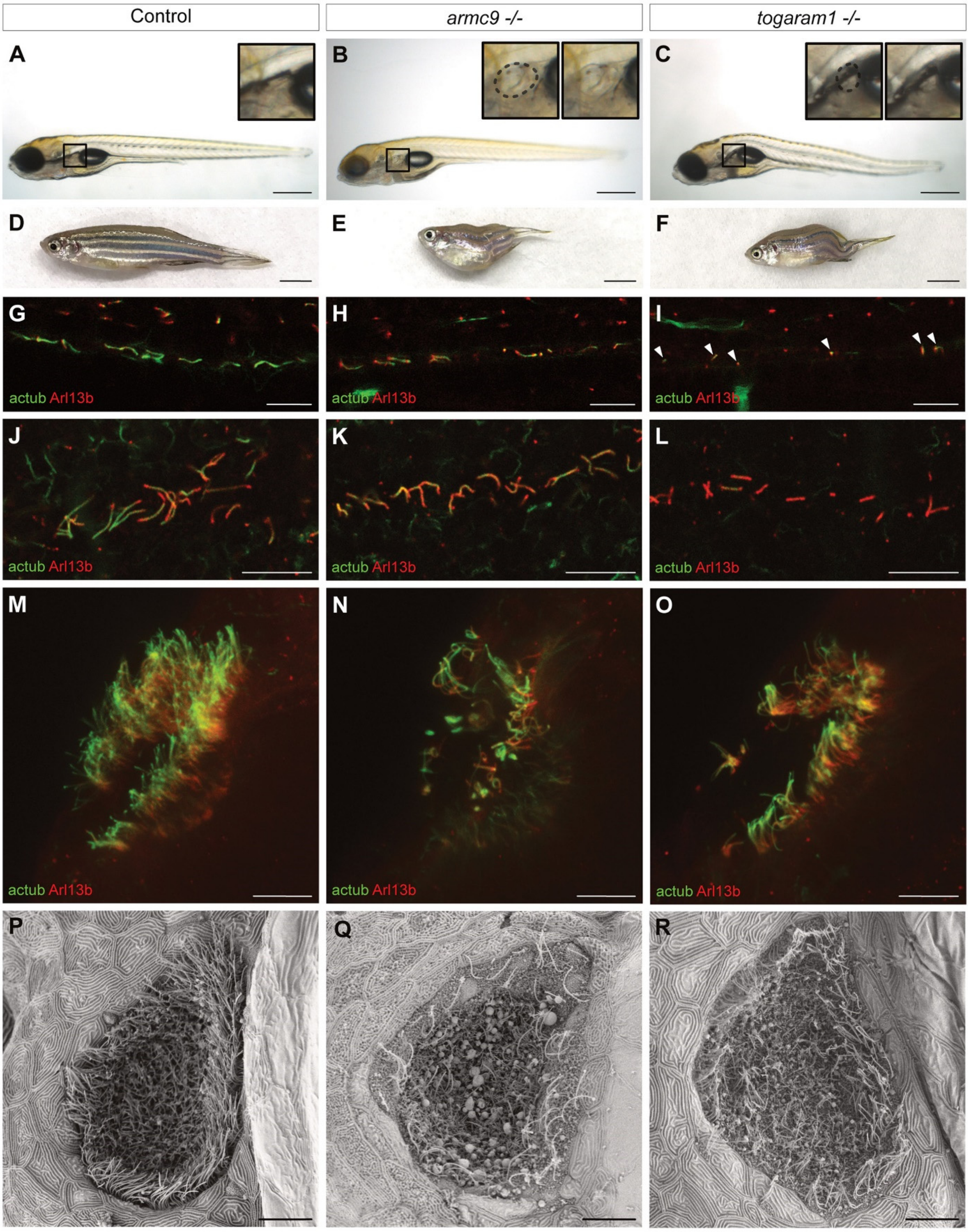

Figure 4 *armc9* and *togaram1* mutant zebrafish display ciliopathy associated phenotypes. **(A-C)** Larval phenotype demonstrating kidney cysts in *armc9*-/- (B) and kidney cysts and slightly curved body shape in

togaram1-/- (C). Black boxes in (A-C) show magnification of glomerulus region in inset. Dashed lines highlight kidney cysts in (B, C). **(D-F)** Adult scoliosis phenotype in both mutants (E, F) compared to wild-type (D). **(G-I)** Immunofluorescence of the pronephric duct in 3 day post fertilization (dpf) larvae showing fewer cilia. White arrowheads in (I) point to the short remaining cilia in the *togaram1* mutant. **(J-L)** Immunofluorescence of midbrain ventricles shows shortened cilia in 3 dpf *armc9* and *togaram1* mutant zebrafish larvae (K, L). **(M-O)** Immunofluorescence of 3 dpf zebrafish nose pits: decreased cilia number in both mutants (N, O) compared to wildtype (M). **(P-R)** Scanning electron microscopy of 5 dpf zebrafish nose pits confirming reduced cilia numbers in *armc9*-/- (Q) and *togaram1*-/- (R). Controls are wildtype, +/+ or +/- siblings of -/-. Scale bars are 500µm in (A-C), 5mm in (D-F) and 10µm in (G-R).

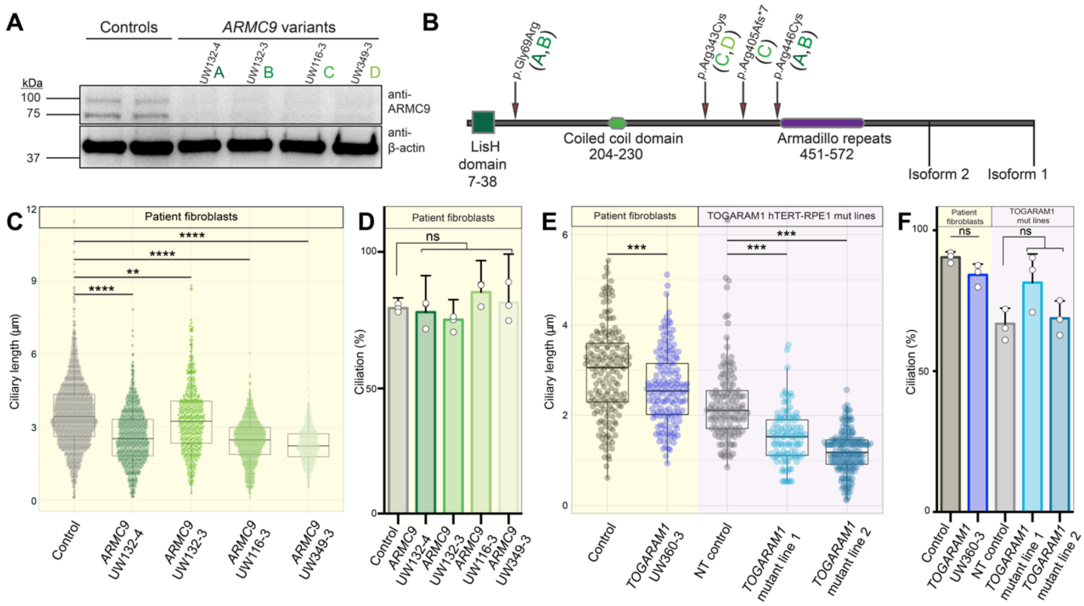

Figure 5 ARMC9 and TOGARAM1 dysfunction results in short cilia. **(A)** Immunoblot of endogenous ARMC9 in control and patient fibroblasts indicating trace amounts of ARMC9 isoforms 1 and 2 (92 and 75.5 kDa). Loading control is β-actin. **(B)** ARMC9 schematic indicating JBTS-associated patient variants (green letters represent variants found in patients as indicated in (A)). **(C)** Ciliary length in control and *ARMC9* patient fibroblasts (control n=1395, UW132-4 n=699, UW132-3 n=437, UW116-3 n=656, and UW349-3 n=353). Significance was assessed by one-way ANOVA with Dunnett's multiple testing correction. **(D)** Ciliation percentage in *ARMC9* fibroblast lines (control n=1723, UW132-4 n=898, UW132-3 n=584, UW116-3 n=764, and UW349-3 n=425). Results were not significant using the Kruskal-Wallis test. **(E)** Ciliary length in control and *TOGARAM1* patient fibroblasts (yellow panel). p=0.0003 using unpaired Student's t-test. hTERT-RPE1 cilia length in wild-type and *TOGARAM1* mut lines (purple panel) based on ARL13B staining. >100 cilia were pooled from 2 experiments (control n=137, *TOGARAM1* mutant line 1 n=111, and *TOGARAM1* mutant line 2 n=178). p<0.0001 per one-way ANOVA with Dunnett's multiple testing correction. **(F)** Ciliation percentage in *TOGARAM1* patient fibroblasts (yellow panel: control n= 466 and UW360-3 n= 429 over 3 experiments), results were not significant using the Mann-Whitney test. Ciliation percentage in engineered *TOGARAM1*-mutant hTERT-RPE1 cells (purple panel: control n=330, *TOGARAM1*

mutant line 1 n=363, and TOGARAM1 mutant line 2 n=357 over 3 experiments) Results were not significant using the Kruskal-Wallis test. Open circles represent individual experiments in (D) and (F). Box and whiskers in (C) and (E) represent the median, the 95 CI is indicated by the notches. All ciliary length measurements were based on ARL13B staining. P-value symbols: ns $p>0.05$, **$p \leq 0.01$, ****$p \leq 0.0001$.

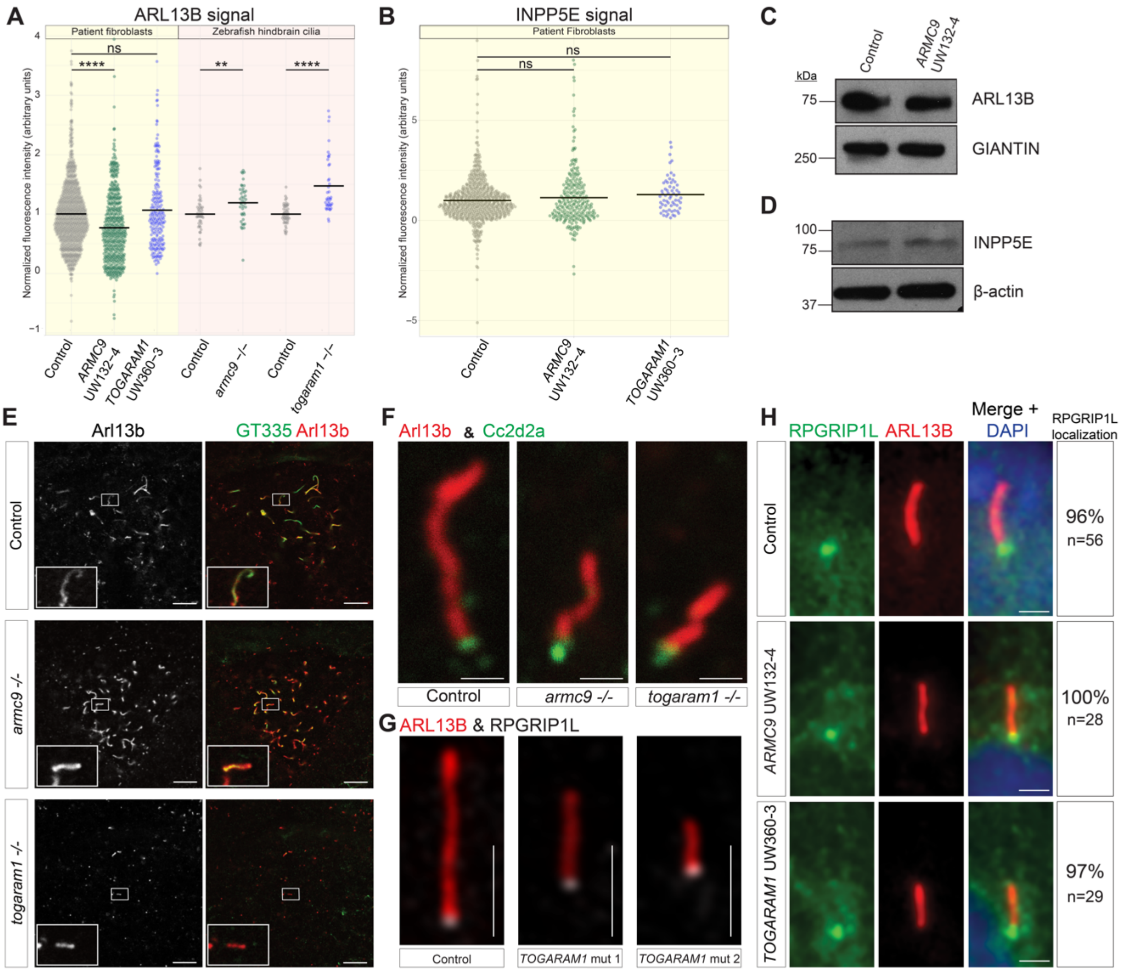

Figure 6 ARMC9 or TOGARAM1 dysfunction does not grossly affect the transition zone. **(A)** Normalized relative fluorescence intensity of ARL13B signal in human fibroblast cilia (yellow panel, pooled from 3 experiments, control: grey n=1089, *ARMC9*: green n=582, and *TOGARAM1*: blue n=126) and 3dpf zebrafish hindbrain cilia (pink panel: pooled data from 4 experiments, 10 cilia measured per larva, each data point represents one larva, grey: *armc9* control n=42, green: *armc9* -/- n=41, grey: *togaram1* control n=45, blue: *togaram1* -/- n=40). Bars represent the mean. Controls are wildtype, +/+ or +/- siblings of -/-. Statistical significance was assessed using a Student's t-test for both fibroblast (Bonferroni adjusted p<0.025) and zebrafish experiments (p <0.05). P-value symbols: **p≤0.01, ****p≤0.0001. **(B)** Normalized relative fluorescence intensity of INPP5E signal in human fibroblast cilia (pooled data from 3 experiments: control:

grey n=620, *ARMC9*: green n=248, *TOGARAM1*: blue n=62). See Supplemental Figure 7 for ARL13B and INPP5E signal intensity across all *ARMC9* fibroblast lines. Results were not significant (ns) using unpaired Student's t-test. **(C-D)** Western blot analysis of ARL13B (C) and INPP5E (D) in *ARMC9* UW132-4 patient fibroblasts. GIANTIN and β-actin serve as loading controls respectively. **(E)** Representative immunofluorescence signal for Arl13b (red) and polyglutamylated (green) in 3dpf zebrafish hindbrain cilia quantified in (A). Scale bars are 10µm. **(F)** Single hindbrain cilia stained with Arl13b (red) and Cc2d2a (green) in 3dpf control, *armc9-/-* and *togaram1-/-* zebrafish. Scale bars are 1µm. **(G)** Representative immunofluorescence signal for RPGRIP1L (white) and ARL13B (red) in cilia from control and two *TOGARAM1*-mutant hTERT-RPE1 lines. Scale bars are 2µm. **(H)** Representative immunofluorescence for RPGRIP1L (green) and ARL13B (red) in *ARMC9* and *TOGARAM1* patient fibroblasts. Percentage of cilia with robust RPGRIP1L puncta are indicated. Scale bars are 2µm.

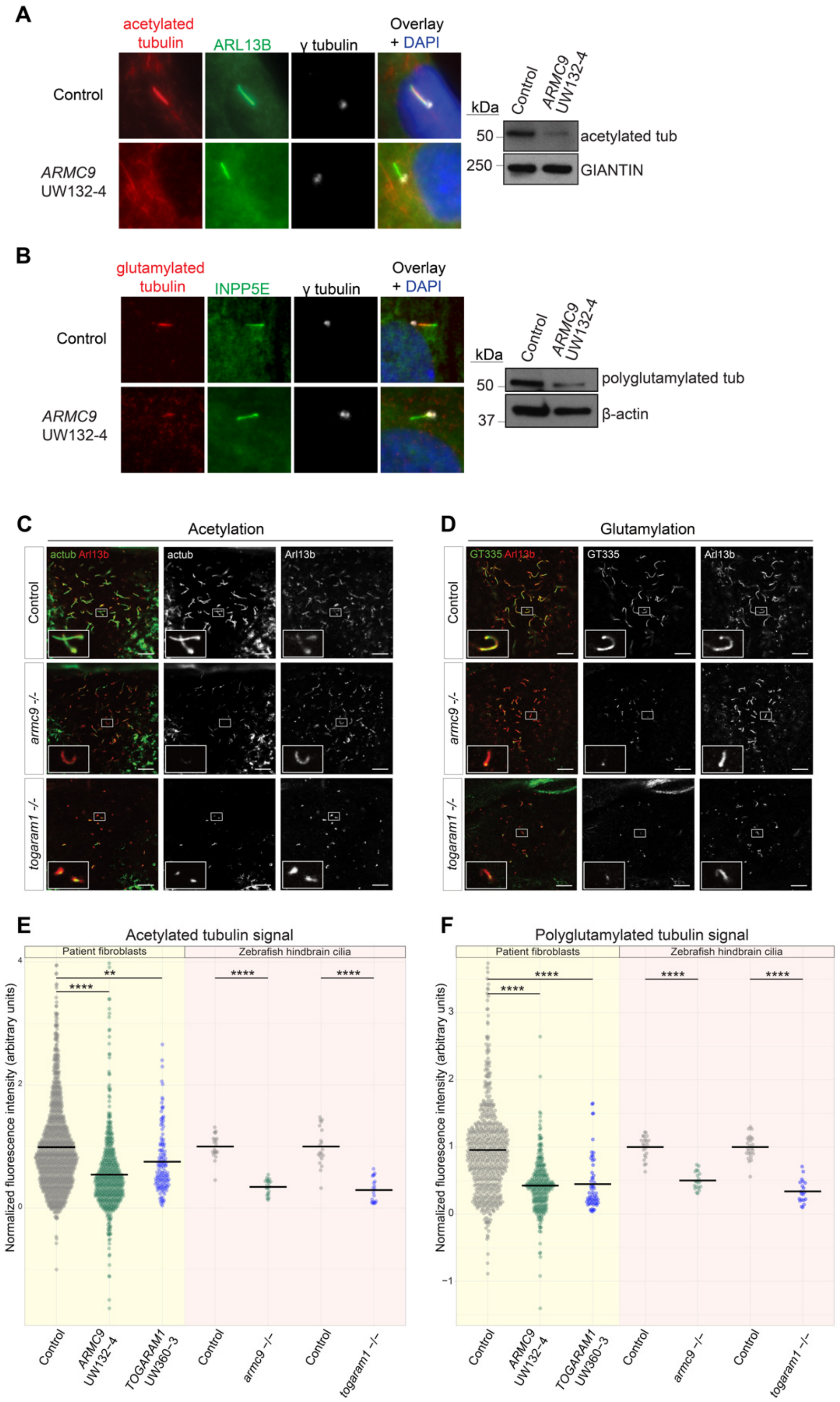

Figure 7 ARMC9 and TOGARAM1 mutant cilia display reduced tubulin posttranslational modifications in both patient fibroblasts and zebrafish ventricular cells. **(A–B)** Immunofluorescence and immunoblots of

(A) acetylated and (B) polyglutamylated tubulin in *ARMC9* patient fibroblasts versus control. In the immunoblots, GIANTIN and β-actin are used as loading controls. **(C-D)** Representative immunofluorescence of 3dpf zebrafish hindbrain cilia marked with Arl13b (red) and acetylated (green in (C)) or polyglutamylated (green in (D)) tubulin. Scale bars are 10µm. Note that acetylated tubulin also marks axons in the developing brain, visible at the edges of the image in (C). **(E)** Normalized relative fluorescence intensity for acetylated tubulin signal in human fibroblast cilia (yellow panel: control n=1106, *ARMC9* n=532, and *TOGARAM1* n=131) and zebrafish hindbrain cilia (pink panel: pooled data from 2 experiments, 10 cilia measured per larva, each data point represents one larva, grey: *armc9* control n=20, green: *armc9* -/- n=21, grey: *togaram1* control n=20, blue: *togaram1* -/- n=20). **(F)** Normalized relative fluorescence intensity for polyglutamylated tubulin assessed in human fibroblast cilia (yellow panel: pooled from 3 experiments, control n=602, *ARMC9* n=298, and *TOGARAM1* n=58) and zebrafish hindbrain cilia (pink panel: pooled data from 2 experiments, 10 cilia measured per larva, grey: *armc9* control n=22, green: *armc9* -/- n=20, grey: *togaram1* control n=25, blue: *togaram1* -/- n=20). Zebrafish controls are wt, +/+ or +/- siblings of -/-. In (E and F), data points >4 and <-2 are not displayed, but were included in the statistical analysis. For complete graph of all data points and a graphical summary of all *ARMC9* lines, see Supplemental Figure 8 (A, B) and (C, D) respectively. Statistical significance (adjusted $p<0.025$) was assessed using a Bonferroni-corrected Student's t-test for both fibroblast and zebrafish experiments. P-value symbols: $^{**}p \leq 0.01$, $^{****}p \leq 0.0001$.

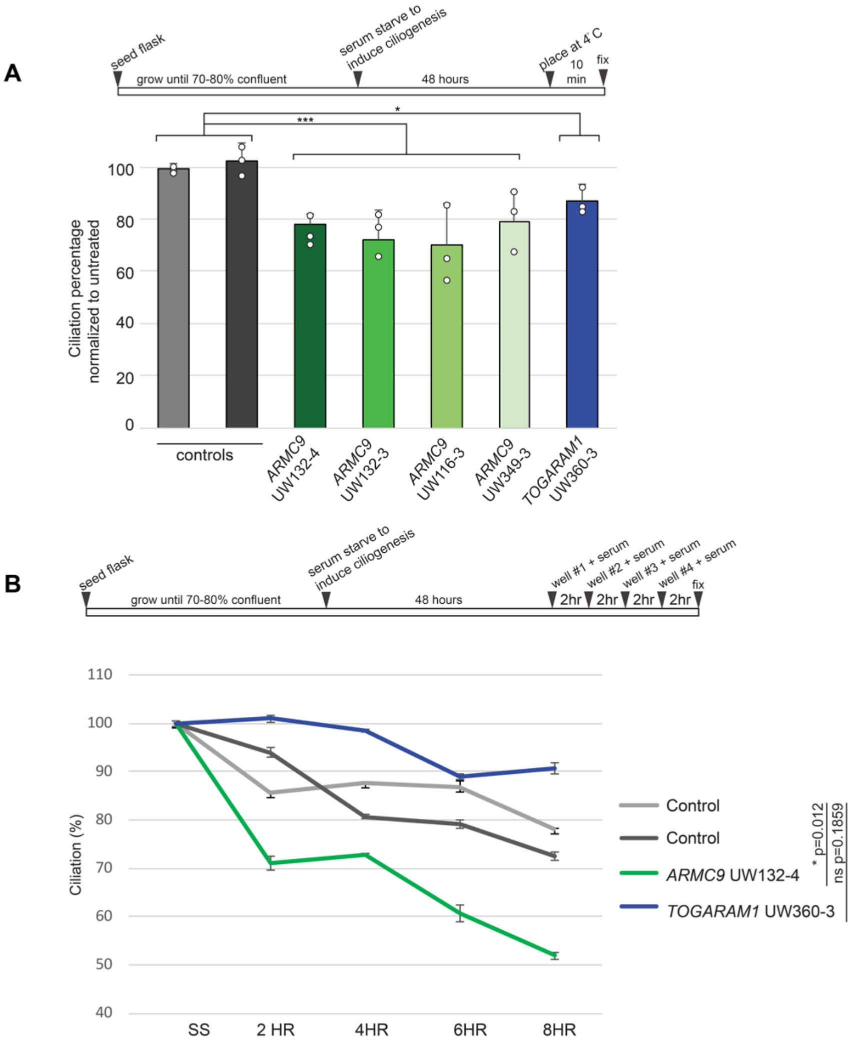

Figure 8 JBTS patient fibroblasts exhibit abnormal axonemal stability. **(A)** Cold-induced depolymerization assay schematic and ciliation percentages of treated cells normalized to non-treated controls. Statistical significance was assessed via Bonferroni-corrected Kruskal-Wallis test with p=0.0003, p=0.02 respectively. Open circles represent individual experiments. **(B)** Relative ciliation rates 2, 4, 6, and 8 hours after serum readdition in human fibroblasts previously serum starved for 48 hours. At t= 0, 2, 4, 6, 8 HR respectively, the following number of cells were assessed: Control 1: 455, 413, 350, 346, 395; Control 2: 595, 431, 351, 368, 279; *ARMC9* UW132-4: 218, 193, 229, 195, 189; *TOGARAM1* UW360-3: 496, 622, 513, 558, 492. Ciliation percentages were normalized to 100% at the time of serum readdition, percentages represent

the amount of remaining cilia compared to time zero. Error bars represent 95% confidence intervals. See "Statistics and reproducibility" section for details of statistical testing for cilia stability assays.

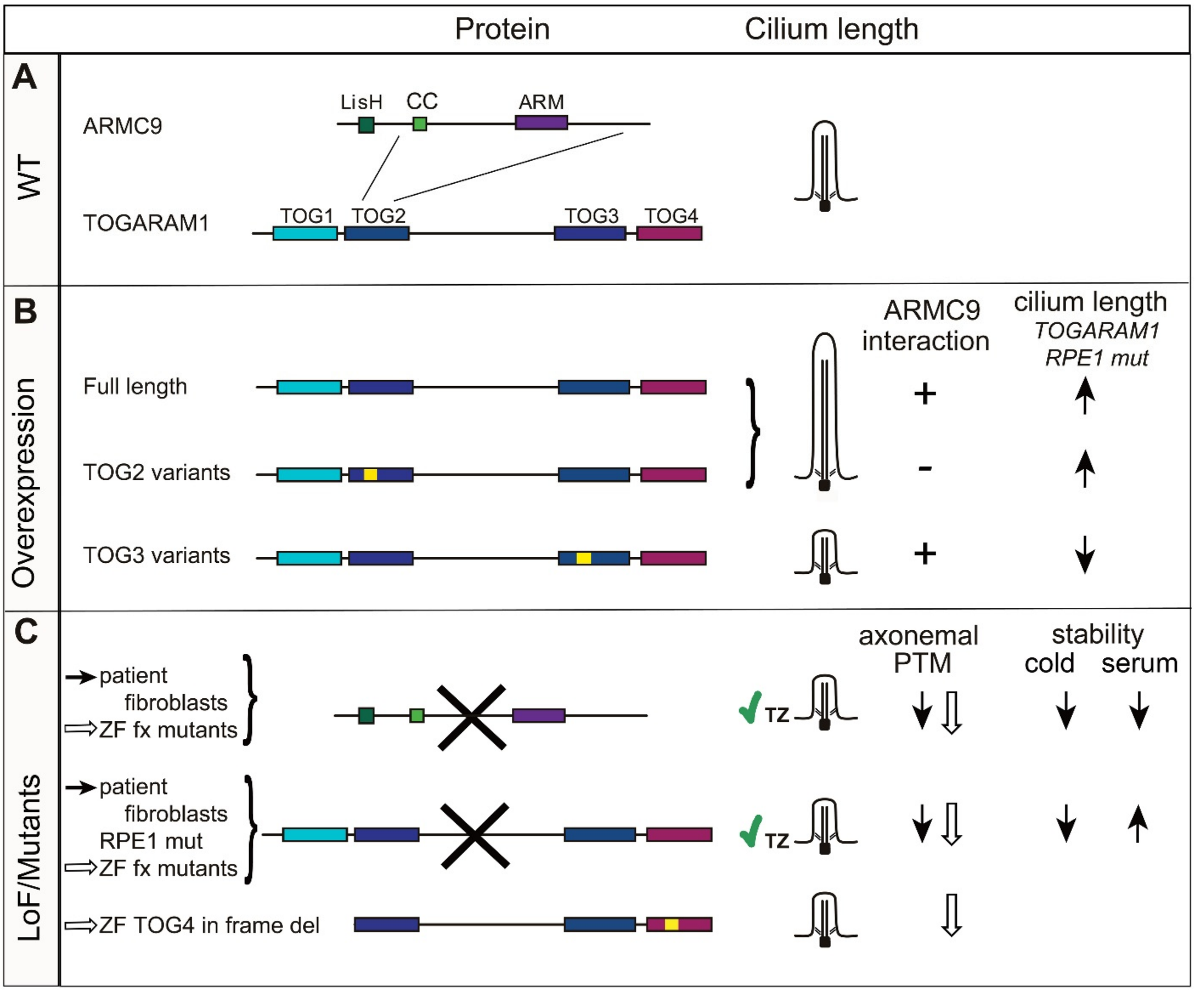

Figure 9 Graphical Summary: Disruptions of the ARMC9-TOGARAM1 module affect ciliary length, axonemal PTMs, and stability. **(A)** TOGARAM1 interacts with ARMC9 through its TOG2 domain. **(B)** Effects of TOGARAM1 overexpression (wild-type and with JBTS-associated variants) on ciliary length in *TOGARAM1* mutant hTERT-RPE1 cells and consequences of JBTS-associated variants on the interaction with ARMC9. **(C)** Consequences of mutations in *ARMC9* or *TOGARAM1* on ciliary length and axonemal post-translational microtubule modifications (PTM) in patient fibroblast lines (black arrows) or zebrafish mutants (white arrows). Transition zone (TZ) integrity despite *ARMC9* or *TOGARAM1* dysfunction is indicated with a green checkmark. Consequences of *TOGARAM1* and *ARMC9* mutations on ciliary stability in response to cold or serum readdition in patient fibroblasts are indicated with black arrows. Yellow boxes

represent pathogenic variants. Bold crosses indicate presumed loss-of-function mutations. del=deletion, fx=frameshift, LoF=loss of function, WT=wild-type, ZF=zebrafish. RPE1 mut=hTERT-RPE1 TOGARAM1 mutant lines. Protein domains: LisH=Lis-homology, CC=coiled-coil, ARM=armadillo, TOG=tumour overexpression gene.

Table 1. Variants and Clinical Features in individuals with *TOGARAM1*-related Joubert syndrome

	UW351-3	**UW360-3**	**13DG1578**	**WGL-1914**	**JAS-L50**
Variant 1^1	c.1124T>C; p.(Leu375Pro)	c.1084C>T; p.(Gln362*)	c.1102C>T; p.(Arg368Trp)	c.3248C>A; p.(S1083*)	c.1112C>A; p.(Ala371Asp)
Allele frequency 1^2	8/276914	0/251328	0/251284	0	5/282580
CADD v1.3^3	25.5	35	28.7	38	26.6
Parent	father	Mother	NA	NA	mother
Variant 2^1	c.3931C>T; p.(Arg1311Cys)	del14q21.2: g.45472062-45484253	c.1102C>T; p.(Arg368Trp)	c.3248C>A; p.(Ser1083*)	c.5023C>T; p.(Arg1675*)
Allele frequency 2	0/218738	NA	0/251284	0	1/251414
CADD v1.3^3	35	NA	28.7	38	NA
Parent	mother	father	NA	NA	NA
Ethnicity/country	Mixed European (Australia)	Mixed European (US)	Middle Eastern (Egypt)	Middle Eastern (Iran)	White British
Gender	male	male	male	male	female
Age	21 wk fetus	16 yr	11 yr, 5 mo	6 yr	14 yr
Molar tooth	VH	Y	Y	Y	Y
Dev disability	NA	Y	Y	Y	Y
Apnea/tachypnea	NA	N	Y	NA	NA
Abnl eye mvts	NA	Y (and strabismus)	Y	NA	Y
Retinal	NA	N	N	NA	N
Kidney	NA	N	N	Y	Y
Liver	NA	N	N	Y	N
Polydactyly	Y (B post-ax foot)	N	N	Y (B post-ax hand)	N
Coloboma	NA	N	N	Y	N
Craniofacial	broad nasal bridge, post rotated ears, thickened neck	low set ears, high arched palate	broad nose, anteverted alae, deep set eyes, hypertelorism, metopic ridge,	broad nasal bridge, anteverted alae, deep set eyes, hypertelorism, frontal bossing	Oculomotor apraxia, Bilateral ptosis, left jaw/ wink ptosis

			frontal bossing, low set ears		
Other		widely spaced nipples, undescended testes, possible micropenis	widely spaced nipples, small scrotum and testes	corpus callosum hypoplasia, neonatal metabolic acidosis and jaundice, hepatomegaly, cholestasis, bilateral hydronephrosis hypotrichosis, small scrotum and testes, possible micropenis, microphthalmia, coloboma	short stature, generalized hypotonia, lumbar hyperlordosis, obesity, joint hypermobility, nonverbal, autistic behaviors, small scarred left kidney

[1] NM_015091.2

[2] gnomAD reference

[3] CADD reference

Abbreviations: Abnl=Abnormal, B=bilateral, mo=months, mvts=movements, N=No, NA=Not Available, post-ax=post-axial, US=United States, VH=Vermis Hypoplasia, wk=weeks, Y=Yes, yr=years